

Naval Research Laboratory

Washington, DC 20375-5000



2

NRL Memorandum Report 6856

AD-A239 531

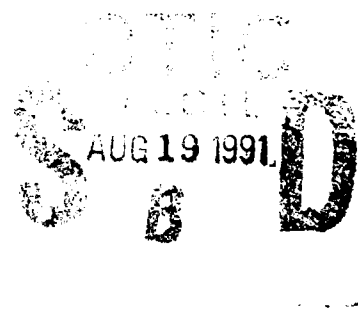


Modelling the Response of Thick Composite Materials Due to Axisymmetric Shock Loading

J. A. NEMES AND P. W. RANGLES

*Mechanics of Materials Branch
Materials Science and Technology Division*

August 5, 1991



91-07996



Approved for public release; distribution unlimited.

91 7 9

REPORT DOCUMENTATION PAGE			Form Approved OMB No 0704-0188	
<small>Public reporting burden for this collection of information is estimated to average 1 hour per response, including the time for reviewing instructions, searching existing data sources, gathering and maintaining the data needed, and completing and reviewing the collection of information. Send comments regarding this burden estimate or any other aspect of this collection of information, including suggestions for reducing this burden, to Washington Headquarters Services, Directorate for Information Operations and Reports, 1215 Jefferson Davis Highway, Suite 1204, Arlington, VA 22202-4302, and to the Office of Management and Budget, Paperwork Reduction Project (0704-0188), Washington, DC 20503.</small>				
1. AGENCY USE ONLY (Leave blank)		2. REPORT DATE 1991 August 5		3. REPORT TYPE AND DATES COVERED
4. TITLE AND SUBTITLE Modelling the Response of Thick Composite Materials Due to Axisymmetric Shock Loading			5. FUNDING NUMBERS PE - 63569E PR - DARPA 6604	
6. AUTHOR(S) J. A. Nemes and P. W. Randles				
7. PERFORMING ORGANIZATION NAME(S) AND ADDRESS(ES) Naval Research Laboratory Washington, DC 20375-5000			8. PERFORMING ORGANIZATION REPORT NUMBER NRL Memorandum Report 6856	
9. SPONSORING / MONITORING AGENCY NAME(S) AND ADDRESS(ES) DARPA Arlington, VA 22209-2308			10. SPONSORING / MONITORING AGENCY REPORT NUMBER	
11. SUPPLEMENTARY NOTES				
12a. DISTRIBUTION / AVAILABILITY STATEMENT Approved for public release; distribution unlimited.			12b. DISTRIBUTION CODE	
13. ABSTRACT (Maximum 200 words) Preliminary efforts for developing a methodology to predict the response of thick composite materials to axisymmetric shock loading are presented. Consideration is given to material layups that result in transversely isotropic behavior in the plane of the fibers. The response of thick graphite/epoxy composite plates subjected to underwater explosive loadings is solved numerically using a transient finite-element code. Both spherical and plane shock waves are considered. Results are compared to analytical results, where possible, along with computed results using steel as the plate material. A continuum damage model appropriate for thick composite materials subjected to high rate loading is developed to consider the response of the composite materials in the nonlinear range. The model considers two different damage parameters, one to represent delamination type cracks and the other to represent matrix cracking. The model is applied initially for different types of homogeneous deformation and then applied to the response of the composite plate subjected to the underwater explosive loading. Computed displacement histories both with and without damage are compared to assess the softening effect of material damage. Damage contours are presented showing the extent of damage to different intensity loadings.				
14. SUBJECT TERMS Composite Shock Damage			15. NUMBER OF PAGES 88	
			16. PRICE CODE	
17. SECURITY CLASSIFICATION OF REPORT UNCLASSIFIED	18. SECURITY CLASSIFICATION OF THIS PAGE UNCLASSIFIED	19. SECURITY CLASSIFICATION OF ABSTRACT UNCLASSIFIED	20. LIMITATION OF ABSTRACT UL	

CONTENTS

I.	INTRODUCTION	1
II.	KINEMATICS AND EQUATIONS OF MOTION	5
III.	CONSTITUTIVE MODEL	7
	Linear Elastic Model	7
	Fluid Modelling	8
IV.	MATERIAL PROPERTIES	10
V.	LOADING CONDITIONS CONSIDERED	11
VI.	NUMERICAL METHODS	14
VII.	NUMERICAL RESULTS FOR SHOCK LOADING	16
	Plane Wave	16
	Spherical Wave on an Infinite Plate	29
	Simply Supported Plate	32
VIII.	DEVELOPMENT OF THE DAMAGE MODEL	42
	Material Description	42
	Damage Description	43
	Material Model	45
	Damage Evolution	48
IX.	DAMAGE MODEL RESULTS FOR HOMOGENEOUS DEFORMATION	53
	Constant Strain Rate Tests	54
	Wave and Spallation Simulation	61
X	PRELIMINARY APPLICATION OF DAMAGE MODEL TO TWO DIMENSIONAL PROBLEMS	69
XI	SUMMARY	77
	REFERENCES	80

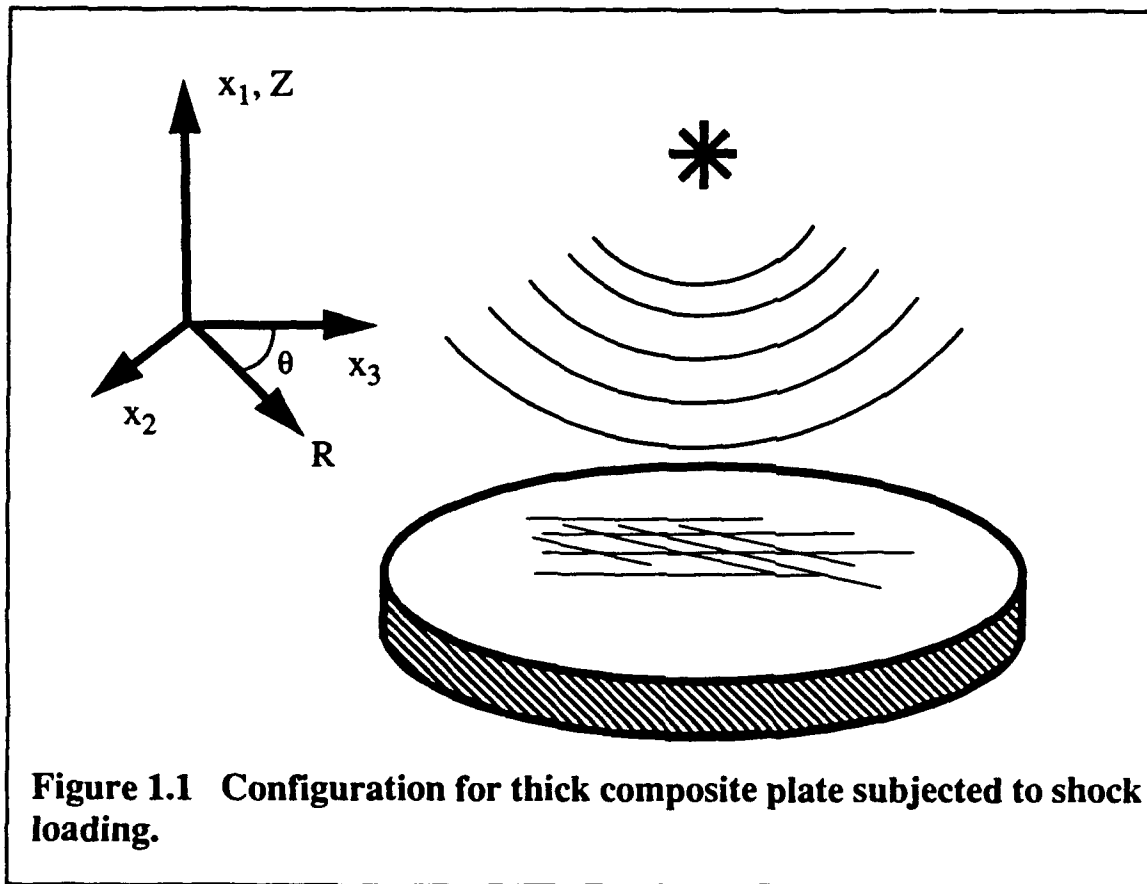
For	
<input checked="" type="checkbox"/>	
<input type="checkbox"/>	
<input type="checkbox"/>	
Date	
Special	
A-1	

MODELLING THE RESPONSE OF THICK COMPOSITE MATERIALS DUE TO AXISYMMETRIC SHOCK LOADING

I. INTRODUCTION

The potential use of thick composite materials for future naval vessels requires an understanding of their response to dynamic loadings such as those arising from impact and underwater explosives. Although numerous investigations have been conducted on the linear vibration of composite plates [1], little has been done in the area of response to extreme transient loadings, particularly when nonlinear behavior associated with material damage is involved. Some work in the area of material response to uniaxial-strain shock loading has been done [2-6], including identification of spallation thresholds. Response of the thick composite due to multi-dimensional deformation type shock loading has received much less attention.

In this report, we report on our preliminary efforts to develop a methodology for predicting the response of thick composite materials to multidimensional shock loadings. Initially we are limiting our consideration to composite material layups that result in transversely isotropic behavior in the plane of the fibers. This assumption along with consideration of loadings that are symmetric about the axis of material symmetry greatly simplifies the fully three-dimensional problem, while still being of both scientific and practical interest. The configuration described above is depicted schematically in Figure 1.1. A principal practical interest in this configuration arises in the



study of the explosive bulge test (EBT). The EBT has been used over a long history [7] to study the deformation and fracture behavior of ship steels under high rate loadings, particularly the behavior of weldments [8]. The use of the test continues today [9-10]. Several current studies are underway to use a form of the EBT to study the response of composite materials to shock loading [11,12].

Although a complete description of the EBT is not part of the scope of this paper, it will briefly be described here. The majority of the tests are conducted underwater since the water can effectively transmit the shock to the plate surface, and because of its apparent similarity to actual conditions experienced by structural components subjected to underwater explosives. The plate to be tested is supported on an anvil having a circular hole in a manner such that the rear surface of the plate is evacuated. An explosive is placed at a given

standoff from the submerged side of the plate and detonated electrically. Instrumentation used during the tests varies somewhat, but recording of deflection histories of the plate, pressure histories at the front surface, and strain histories at the rear surface are common.

The material and loading symmetries considered in this paper have practical interest beyond the consideration of the EBT. In cases where actual configuration of naval components is such that the layup is transversely isotropic (or nearly so), the local response to such events as torpedo impact or shock wave due to a nearby explosive can be appropriately treated using the configuration considered here as long as the offset distance is much smaller than the radius of the shell being considered and the events of interest occur during times such that the outer boundaries can be appropriately considered.

In Section II, the kinematics associated with the configuration discussed above are developed along with the equations of motion in the cylindrical coordinate system specialized for axisymmetric deformation. Section III contains the development of the material constitutive model. In this preliminary investigation, the laminated composite material is idealized as a transversely isotropic, homogeneous linear solid. The subsequent development of a nonlinear damage model and its applications are presented in later sections. Material properties are discussed in Section IV. The computations presented here have been performed using graphite/epoxy as the model material, both because of present interest in the material and its fairly extensive characterization at least under static loading conditions. Under high loading rates, however, experimental data on the material behavior is sparse [13,14]. Section V provides a brief discussion of loading associated with underwater explosives. For the purposes of this report, use is made of empirical formulas to determine amplitude and shape of the shock wave

loading. A discussion of the numerical method used is included in Section VI. Explicit integration of the balance equations of mass and momentum is performed using the computer code PRONTO-2D [15]. Several sample problems are considered in Section VII to illustrate the methodology considered for shock response of thick composites. The development of the damage model is contained in Section VIII and several cases of homogeneous deformation are considered in Section IX. Finally, preliminary application of the damage model to the multi-dimensional response to shock loading is considered in Section X.

II. KINEMATICS AND EQUATIONS OF MOTION

The kinematics to describe the deformation associated with the configuration shown in Figure 1.1 is presented in this section. The reference configuration of the body is defined by particles that occupy position \underline{X} in that configuration. The current configuration, \underline{x} , is defined by the motion, $\underline{\chi}$, such that

$$\underline{x} = \underline{\chi}(\underline{X}, t) . \quad (2.1)$$

Taking the time derivative of (2.1), holding \underline{X} fixed, defines the material velocity

$$\underline{v} = \dot{\underline{x}} = \left(\frac{\partial}{\partial t} \underline{\chi}(\underline{X}, t) \right)_{\underline{X}} . \quad (2.2)$$

The velocity gradient

$$\underline{L} = \frac{\partial \underline{v}}{\partial \underline{x}} \quad (2.3)$$

can be decomposed into symmetric and anti-symmetric parts

$$\underline{L} = \underline{D} + \underline{W} , \quad (2.4)$$

where the skew symmetric tensor \underline{W} is the spin tensor. For small strains $\underline{D} \sim \underline{\epsilon}$ so that the strain tensor is defined by

$$\underline{\epsilon} = \int_0^t \underline{D} dt' . \quad (2.5)$$

Referring to cylindrical coordinates, $\underline{X} = (X^1, X^2, X^3) = (Z, R, \Theta)$ and $\underline{x} = (x^1, x^2, x^3) = (z, r, \theta)$, for axisymmetric deformation where the motion is independent of Θ , $\underline{\chi} = \underline{\chi}(Z, R, t)$. The strain tensor, therefore has non-zero components ϵ_{11} , ϵ_{22} , ϵ_{33} , and $\epsilon_{12} = \epsilon_{21}$, all of which are independent of θ .

The balance of mass requires that

$$\frac{\rho_R}{\rho} = J \quad (2.6)$$

where $\rho(\underline{x}, t)$ and $\rho_R(\underline{X})$ are the mass densities in the current and reference

configuration respectively and J is the Jacobian of the deformation. Balance of linear momentum leads to the equation of motion

$$\text{div} \underline{\sigma} + \rho \underline{b} = \rho \frac{d\underline{v}}{dt}, \quad (2.7)$$

which, for axisymmetric deformation (neglecting the body force \underline{b}), reduces to

$$\frac{\partial \sigma_{rr}}{\partial r} + \frac{\partial \sigma_{rz}}{\partial z} + \frac{1}{r} (\sigma_{rr} - \sigma_{\theta\theta}) = \rho \frac{dv_r}{dt} \quad (2.8)$$

$$\frac{\partial \sigma_{rz}}{\partial r} + \frac{\partial \sigma_{zz}}{\partial z} + \frac{1}{r} \sigma_{rz} = \rho \frac{dv_z}{dt}.$$

III. CONSTITUTIVE MODEL

Linear Elastic Model

The generalized Hooke's Law relating stress and strain can be written as

$$\underline{\sigma} = \underline{C}\underline{\epsilon} \quad (3.1)$$

where \underline{C} is the fourth-order elasticity tensor, which for completely anisotropic materials contains 21 independent components. Materials containing three planes of symmetry are termed orthotropic and contain 9 independent components. In addition, if there is one plane in which mechanical properties are equal in all directions, the material is transversely isotropic and the number of independent material constants is reduced to five.

The composite material under consideration is *idealized* as transversely isotropic thus requiring specification of only the five components. Considering the axisymmetric deformation discussed in Section II, Equation (3.1) can be written as

$$\begin{bmatrix} \sigma_{11} \\ \sigma_{22} \\ \sigma_{33} \\ \sigma_{12} \end{bmatrix} = \begin{bmatrix} C_{11} & C_{12} & C_{12} & 0 \\ C_{12} & C_{22} & C_{23} & 0 \\ C_{12} & C_{23} & C_{22} & 0 \\ 0 & 0 & 0 & C_{44} \end{bmatrix} \begin{bmatrix} \epsilon_{11} \\ \epsilon_{22} \\ \epsilon_{33} \\ \epsilon_{12} \end{bmatrix} \quad (3.2)$$

where the contracted notation has been used for the fourth order tensor \underline{C} . The components of \underline{C} given in terms of the engineering properties are

$$\begin{aligned} C_{11} &= \frac{(1 - \nu_{23}) E_{11}}{1 - \nu_{23} - (2\nu_{12}^2 E_{22}) / E_{11}} \\ C_{22} &= \frac{[1 - (\nu_{12}^2 E_{22}) / E_{11}] E_{22}}{(1 + \nu_{23}) [1 - \nu_{23} - (2\nu_{12}^2 E_{22}) / E_{11}]} \\ C_{12} &= \frac{\nu_{12} E_{22}}{1 - \nu_{23} - (2\nu_{12}^2 E_{22}) / E_{11}} \end{aligned} \quad (3.3)$$

$$C_{23} = \frac{[v_{23} - (v_{12}^2 E_{22}) / E_{11}] E_{22}}{(1 + v_{23}) [1 - v_{23} - (2v_{12}^2 E_{22}) / E_{11}]}$$

$$C_{44} = 2G_{12}.$$

For modelling isotropic materials, only two independent material properties are required. Thus, specification of the Young's modulus, E , and the Poisson's ratio, ν , is sufficient to characterize the linear elastic behavior of the material.

The stress-strain relations are given by

$$\sigma_{ij} = \lambda I_e \delta_{ij} + 2G e_{ij} \quad (3.4)$$

where I_e is the first invariant of the strain tensor, δ_{ij} is the Kronecker delta,

$$\lambda = \frac{E\nu}{(1 + \nu)(1 - 2\nu)}, \quad (3.5)$$

and

$$G = \frac{E}{2(1 + \nu)}. \quad (3.6)$$

Fluid Modelling

For studying problems involving fluid-structure interaction, modelling the fluid using finite elements offers many advantages over using boundary element techniques, such as doubly asymptotic approximations (DAA) [17]. Material nonlinearity as well as cavitation can be addressed fairly easily using finite elements, while either can be modelled only with great difficulty or not at all with boundary element techniques. In studies of material damage it is expected that pressures acting in the fluid will be sufficiently high that the nonlinear fluid behavior is significant. In addition, shock waves propagating in a fluid and impinging on a flat plate in the configuration of Figure 1.1 can be expected to result in cavitation as waves reflect back from the free-rear surface of the solid. The use of non-reflecting boundaries [18,19], discussed in more detail in Section VI, limits the amount of fluid that must be modelled, which is often cited as a drawback in using finite-elements to model fluid

behavior.

The constitutive model for the fluid is taken as a simple hydrodynamical model where

$$\sigma_{ij} = -p\delta_{ij} = K_0\eta (1 + K_1\eta + K_2\eta^2 + \dots) \text{ for } (\eta > 0) \quad (3.7)$$

where $\eta = 1 - \rho_0/\rho$ and $p = 0$ for $\eta < 0$.

IV. MATERIAL PROPERTIES

For the simulations conducted in this report the model material used is for a graphite/epoxy with a transversely isotropic layup. Tsai [16] gives properties for a graphite/epoxy composite composed of T300 fiber with N5208 matrix. The properties given are for ρ , E , and ν , which are the in-plane averaged properties corresponding to E_{22} and ν_{23} , in the notation given in Section III. The properties given are

$$\begin{aligned}\rho &= 1600 \text{ kg/m}^3 \\ E_{22} &= 69.0 \times 10^3 \text{ MPa} \\ \nu_{23} &= 0.30 .\end{aligned}\tag{4.1}$$

The through-thickness modulus E_{11} , the transverse shear modulus, G_{12} , and the ν_{21} Poisson's ratio are assumed to be equal to the transverse modulus, the in-plane shear modulus, and the Poisson's ratio, respectively, of a single ply given in [16], such that

$$\begin{aligned}E_{11} &= 10.3 \times 10^3 \text{ MPa} \\ G_{12} &= 7.17 \times 10^3 \text{ MPa} \\ \nu_{21} &= 0.28 .\end{aligned}\tag{4.2}$$

For comparative simulations involving steel the properties used are

$$\begin{aligned}\rho &= 7779 \text{ kg/m}^3 \\ E &= 206.8 \times 10^3 \text{ MPa} \\ \nu &= 0.30 .\end{aligned}\tag{4.3}$$

Material properties for water, referring to the constitutive model of Section III, are given by (with $K_2=0$)

$$\begin{aligned}\rho &= 998 \text{ kg/m}^3 \\ K_0 &= 2.33 \times 10^3 \text{ MPa} \\ K_1 &= 1.75 .\end{aligned}\tag{4.4}$$

V. LOADING CONDITIONS CONSIDERED

The theory of shock waves from underwater explosion has been extensively treated and is defined primarily by the Kirkwood-Bethe theory [18]. Because of its complexity, however, Kirkwood-Bethe is infrequently used, and it is replaced for the most part by semi-empirical scaling laws such as the Arons [19], which gives the peak pressure of the shock wave in terms of weight of TNT, W , and distance from the center of charge, R . Pressures from other types of explosive are commonly determined by defining them in terms of an equivalent weight of TNT. The scaling law, which has been verified experimentally over several orders of magnitude is given by

$$P_m = K_p (W^{1/3}/R)^{1.13} \quad (5.1)$$

When R is given in meters and W in kilograms, $K_p = 5.19 \times 10^4$ and P_m is given in kilopascals. When R is given in feet and W in pounds, $K_p = 2.16 \times 10^4$ and P_m is given in pounds per square inch. The shape of the shock wave is taken to have an instantaneous rise with an exponential decay. The pressure is then given by

$$P(t) = P_m e^{-\frac{t}{\theta_t}} \quad (5.2)$$

where arrival of the wave is taken to be at $t = 0$. The characteristic time, θ_t , is also given by an Arons scaling law

$$\theta_t = K_t W^{\frac{1}{3}} \left(W^{\frac{1}{3}}/R \right)^{-0.22} \quad (5.3)$$

where θ_t is given in microseconds. $K_t = 92.5$ when R is given in meters and W in kilograms and $K_t = 58$ when R is in feet and W in pounds. Rogers [20] reports that (5.3) has been experimentally verified over a smaller range of values of $(W^{1/3}/R)$. Problems in using the empirical forms given by (5.1) and (5.3) are also noted [10] for small offsets. Nevertheless use of the empirical

forms are sufficient to illustrate the modelling considered in this report, although caution should be used if these empirical forms are used in trying to correlate computed results with experimental data. A range of explosive weights and offset distances is considered in giving the peak pressures and characteristic times in Tables 5.1 and 5.2, developed from (5.1) and (5.3). As

TABLE 5.1 PEAK PRESSURE (PSI) FOR DIFFERENT EXPLOSIVE
WEIGHTS AND OFFSET DISTANCE

<u>R</u> <u>(FT)</u>	<u>W (LBS)</u>						
	<u>10</u>	<u>50</u>	<u>100</u>	<u>500</u>	<u>1000</u>	<u>2000</u>	<u>3000</u>
2	23494	43076	55927	-	-	-	-
5	8342	15295	19859	36411	47273	61377	71504
10	3812	6989	9074	16637	21600	28044	32672
20	1742	3193	4146	7601	9869	12814	14928
50	618	1134	1472	2699	3504	4550	5301
100	283	518	673	1233	1601	2079	2422
200	129	237	307	564	732	950	1107

seen from the tables the peak pressures vary tremendously but the characteristic time is almost entirely in the range of 10^{-4} to 10^{-3} seconds.

TABLE 5.2 CHARACTERISTIC TIME θ_1 (MSEC) FOR DIFFERENT EXPLOSIVE WEIGHTS AND OFFSET DISTANCE

R (FT)	W (LBS)						
	10	50	100	500	1000	2000	3000
2	.1229	.1868	.2237	-	-	-	-
5	.1504	.2285	.2737	.4159	.4980	.5963	.6626
10	.1752	.2662	.3187	.4844	.5800	.6945	.7718
20	.2040	.3100	.3712	.5641	.6756	.8089	.8989
50	.2496	.3793	.4542	.6901	.8264	.9896	1.0996
100	.2907	.4417	.5290	.8038	.9626	1.1526	1.2808
200	.3386	.5145	.6161	.9362	1.1211	1.3425	1.4918

VI. NUMERICAL METHODS

Solution of the balance equations of mass and momentum for the configuration shown in Figure 1.1 is performed numerically, using the finite-element computer code PRONTO-2D [15]. PRONTO-2D is a two-dimensional, explicit integration, finite-element code, developed specifically for solution of transient problems. The code is developed in a Lagrangian formulation [21]. Simple four-noded quadrilateral uniform strain elements, with hourglass control [22] are used for the discretization.

In computing the response to shock loading, that is, a loading that produces a discontinuity in the particle velocity, artificial viscosity [23] must be applied to the numerical procedure. The effect of artificial viscosity is to smear a shock front across several elements, thus replacing the shock front with one that has a rapid but finite rise time. The effect of this smearing of the shock on the solution is discussed further in the following sections.

The numerical procedure employed also makes use of nonreflecting boundary conditions [24, 25]. These boundaries are particularly useful for limiting the extent of fluid to be modelled. Use of a simple free surface would require that a sufficient volume of fluid be modelled such that reflections off that surface do not reflect and impinge again on the body of interest. The use of nonreflecting boundaries, however, are intended to behave as if the fluid extended to infinity while limiting the actual region to be modelled [25]. Implementation of the nonreflecting boundary for the fluid is accomplished by applying tractions normal to the boundary such that the stresses at the surface cancel. The normal stress applied, σ_n , is determined from

$$\sigma_n = \rho c_p v_n \quad (6.1)$$

where ρ is the current fluid density, c_p is the bulk sound speed in the fluid and v_n is the fluid particle velocity in the direction normal to the boundary.

The fluid-solid interface is modelled using a contact surface algorithm in which both media are deformable. The algorithm uses kinematic constraints, in which the accelerations of the nodes along the surface are modified. Final accelerations are computed such that one surface may not penetrate the other, while at the same time establishing constraint forces that conserve momentum. At each time step the motion is first computed without the kinematic constraints to determine the extent of contact between the surfaces. From this computed motion, the penetration forces necessary to satisfy the kinematic constraints are calculated and used to modify the accelerations.

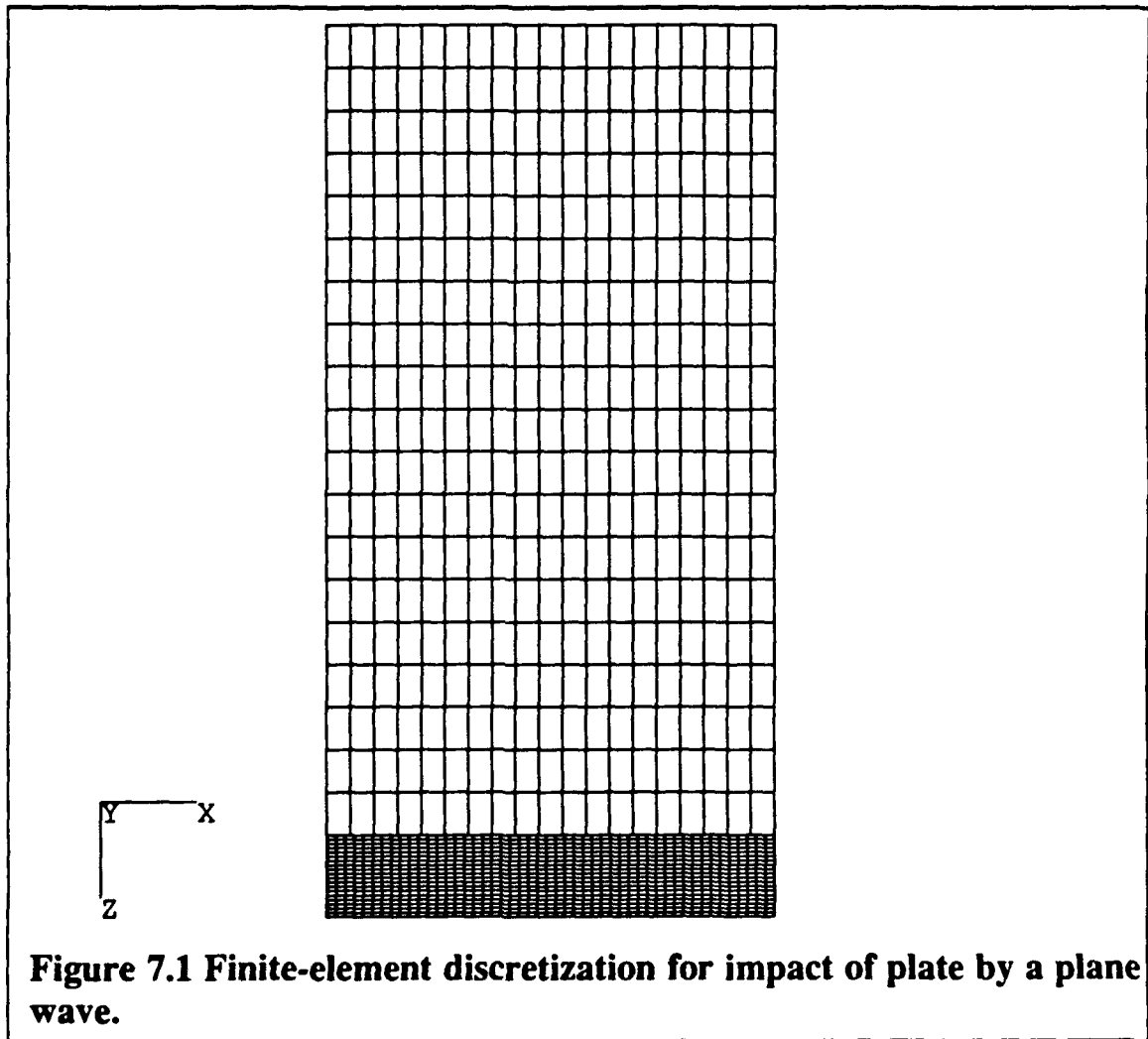
VII. NUMERICAL RESULTS FOR SHOCK LOADING

In this section several sample problems are considered in order to illustrate the methodology considered for addressing the shock response of thick composites under multi-axial loading. The model composite material used is graphite/epoxy with the properties given in Section IV. Several comparisons with steel are presented. Where possible comparisons are also made with analytical solutions. The problems are intended to illustrate various phases of the methodology considered here for evaluating multi-dimensional material response to shock loading, such as fluid-structure interaction, wave propagation through the material, development of tensile stresses in the through-thickness direction of the composite and finite-element discretization.

Plane Wave

The first problem considered is the response of a 25.4 mm thick infinite plate subjected to a plane wave of temporal distribution given by Equation (5.2). Since we are interested in normalizing the response only the linear behavior of the fluid is considered, i.e $K_1=K_2=0$ in Equation (3.7). The characteristic time, θ_1 , is taken to be 0.0001 sec. The finite element model for the problem is shown in Figure 7.1. The model uses a mesh of 19x19 elements for the fluid, which is 254 mm in the z-direction, and 39x19 elements for the plate. The mesh is considered to be fairly coarse and is used here for illustration purposes. The sides given by $r=0$ and $r=r_1$ are constrained such that the velocity $v_r=0$. The plate is free in the z-direction. A uniform spatial pressure is applied to the outer boundary surface of the fluid and the silent boundary condition is also applied to this boundary to prevent reflection of the waves back from the boundary surface after it has reflected off the plate. These boundary and loading conditions result in a uniaxial deformation field, which

could more appropriately be described using a one-dimensional finite-difference technique. The purpose here, however, is to evaluate the use of the two-dimensional finite element modelling technique by comparing results with an analytic solution. The uniaxial deformation allows the problem to be modelled independent of the size of the mesh in the r -direction, thus a fairly narrow slice is used as shown in Figure 7.1.



The analytical solution for the problem described above can be obtained directly from consideration of transient elastic plane waves in an elastic media. The wave profile described by Equation (5.2) travels undisturbed through the fluid at a velocity equal to its sound speed until it encounters the boundary of the plate. At that point a portion of the wave is transmitted and a

portion of it is reflected. The relative fractions of each is governed by the density and wave velocity of the two media. At the boundary between the two media the normal stresses must be equal at every instant of time and the normal particle velocities must be equal. This holds in compression, but when tension develops across the interface, separation of the fluid from the solid occurs. The boundary conditions result in the following relationships between the transmitted, reflected and incident stress wave magnitudes (σ_T , σ_R , and σ_I , respectively)

$$\sigma_T = [(2\rho'c') / (\rho'c' + \rho c)] \sigma_I \quad (7.1a)$$

$$\sigma_R = [(\rho'c' - \rho c) / (\rho'c' + \rho c)] \sigma_I \quad (7.1b)$$

where ρ is the density and c is the wave speed. The primes denote the second medium, which in this case is the solid, and the unprimed quantities are for the fluid. The wave speed for the fluid is given by

$$c = (K_0/\rho)^{1/2} . \quad (7.2)$$

The wave velocity for a transversely isotropic solid is given by

$$c = (C_{11}/\rho)^{1/2} \quad (7.3)$$

or in the case of an isotropic solid by

$$c = [(\lambda + 2G) / \rho]^{1/2} . \quad (7.4)$$

The stress in the fluid is then the sum of the incident and reflected waves and the stress in the solid is that given by the transmitted wave. Examination of Equation (7.1a), in view of the material properties given in Section IV, shows that 1.93 times the incident wave would be transmitted to steel, but only 1.46 times the incident wave would be transmitted to the graphite/epoxy. Implications of this on the ability of the material to withstand shock loading are discussed later.

The transmitted wave propagates through the solid until it encounters the free rear surface. Conditions at this boundary can be obtained from Equations

(7.1a) and (7.1b) by considering the first medium to be the solid (unprimed) and the second medium to have $\rho' c' = 0$. Thus from Equations (7.1a) and (7.1b), the transmitted wave is equal to zero and the reflected wave is equal to $-\sigma_I$. This wave is superimposed with the incident wave in the solid to give the total stress in the solid. By applying these boundary conditions for each interface encountered, the stress history in both the solid and the fluid can be obtained. These analytical results are shown and compared with the finite element calculations to illustrate the effects of discretization and artificial viscosity on numerical accuracy.

Results of the finite-element analysis are given in terms of pressure histories in the fluid or stress histories in the solid at specific points and then compared with the analytical results. The first simulation is for the plane wave impinging on the graphite/epoxy plate. Figure 7.2 shows the computed pressure history at the element adjacent to the centerline ($R=0$) and furthest out in the fluid ($Z = -247.00$ mm). The idealized shock front now has a finite rise and the decay exhibits some oscillations, which are numerical in origin. The rise that occurs after 0.0003 seconds is a result of the reflected wave from the front of the plate. The analytical solution for the same point in space is also given in Figure 7.2. The computed solution agrees well with the analytic solution concerning the magnitude of the initial wave as well as the slope of the decay. The magnitude of the reflected wave is under predicted by the numerical solution. Figure 7.3 shows the pressure history for the element at the middepth ($Z = -113.00$ mm) of the fluid. Spreading of the shock front is more pronounced as are the numerical oscillations in the decay. The rise at 0.00025 seconds is not numerical, but is due to the reflection from the face of the plate. The comparable analytic solution is also given in Figure 7.3. Comparison between the analytic and numerical solutions is reasonable.

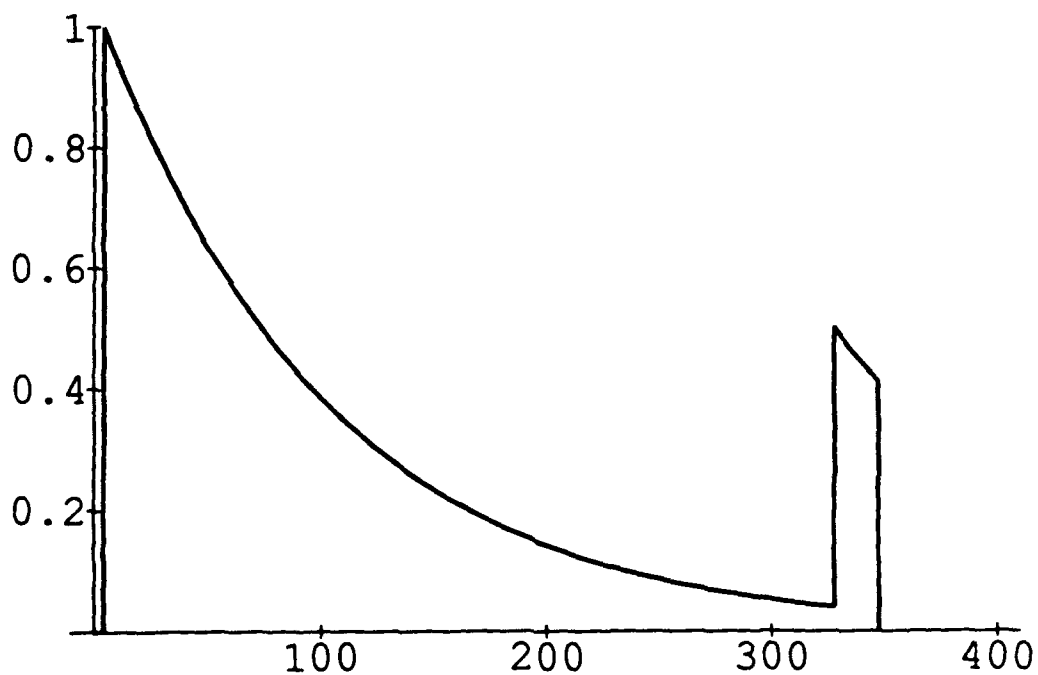
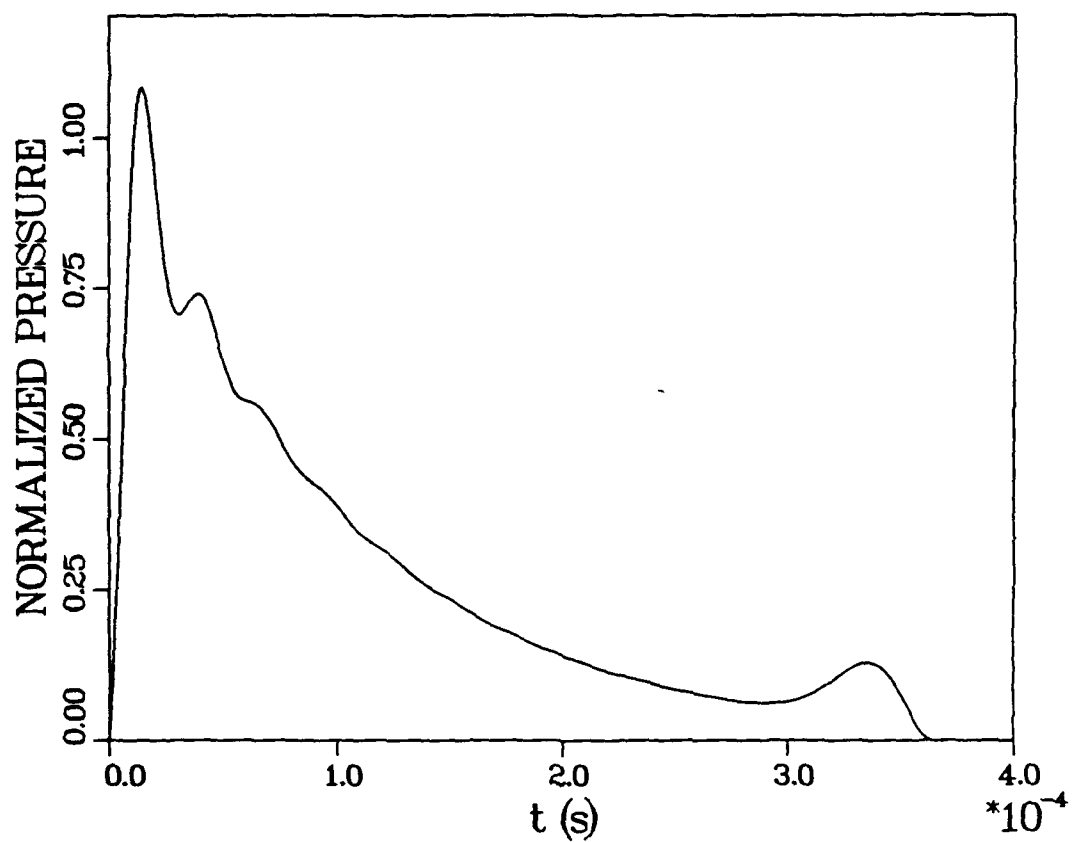


Figure 7.2 Finite-element and analytical results for pressure at the boundary of the fluid due to plane shock wave loading on a graphite/epoxy plate.

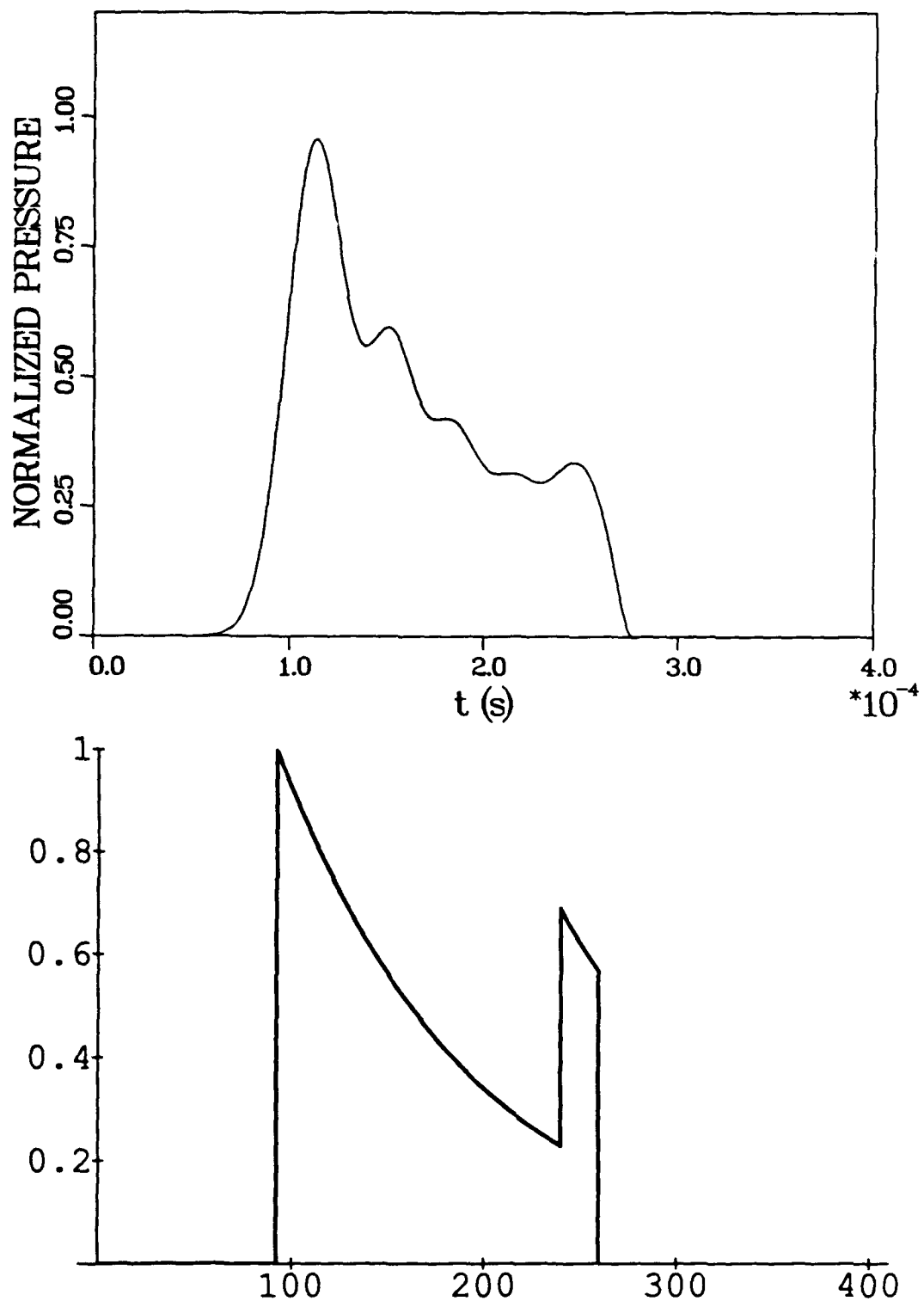


Figure 7.3 Finite-element and analytical results for pressure in the fluid at $z=-113$ mm due to plane wave shock loading on a graphite/epoxy plate.

The history of the normal component of stress in the z-direction in the solid at the element closest to the interface ($Z = 0.67$ mm) with the fluid is shown in Figure 7.4. The analytic solution is also given in Figure 7.4. Comparison of the two shows that the finite-element solution under predicts the peak compressive stress reached at the surface of the plate. The duration of the compressive pulse, which is directly related to the travel time through the thickness of the plate, is longer in the numerical solution. The reason for both of these findings can be traced to the spreading of the shock rise as the wave propagates through the fluid and subsequently the solid. The similar stress history for a point at mid-thickness of the plate ($Z = 14.04$ mm) is shown in Figure 7.5 for the finite-element and analytic solution, respectively. Here the under prediction of the compressive stress in the solid is quite significant and also significant is the fact that the analytical solution is predicting the existence of fairly large tensile stresses that are almost negligible in the numerical solution. As seen in comparing the two results is that the frequency of the oscillations is quite similar between the two with the principal difference being that the numerical solution is rounding off the wave profiles that are sharp and distinct in the analytical solution.

For the purposes of comparison, a second simulation conducted using steel as the plate material is presented. Pressure history results in the fluid from both the finite-element analysis and the analytical solution are given in Figure 7.6 and Figure 7.7. The principal difference to note in the pressure histories at the two points in the fluid is the much larger reflected wave that occurs at both points in the fluid. The stress history near the plate interface, in Figure 7.8 shows that the maximum compressive stress reached is higher than that in the graphite/epoxy as discussed above. The computed stress at midplane, shown in Figure 7.9 significantly under predicts the maximum compressive stress shown in the analytical solution. This is more severe than in the case of the

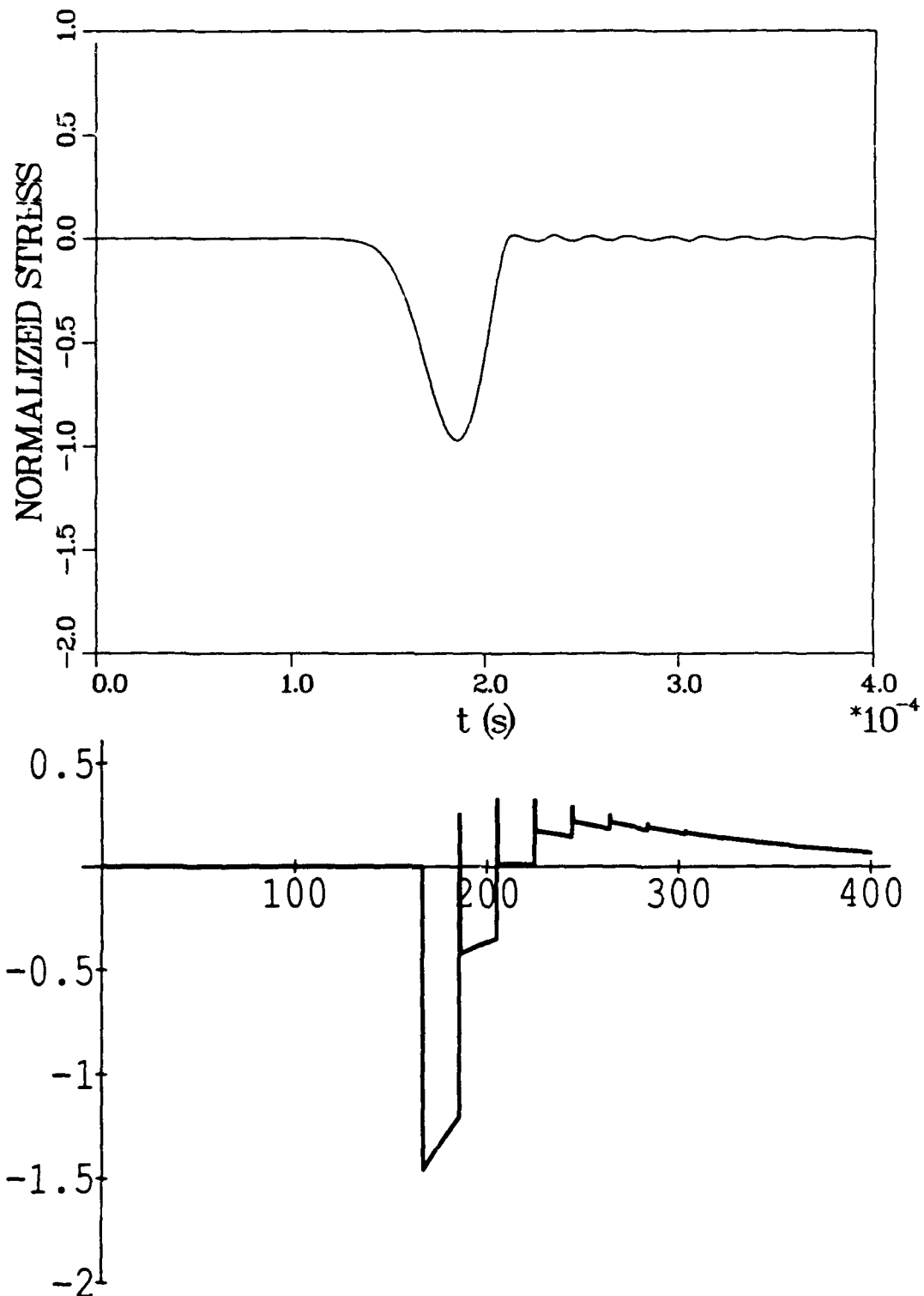


Figure 7.4 Finite-element and analytical results for σ_{zz} near the solid-fluid interface for the graphite/epoxy plate subjected to plane shock wave loading.

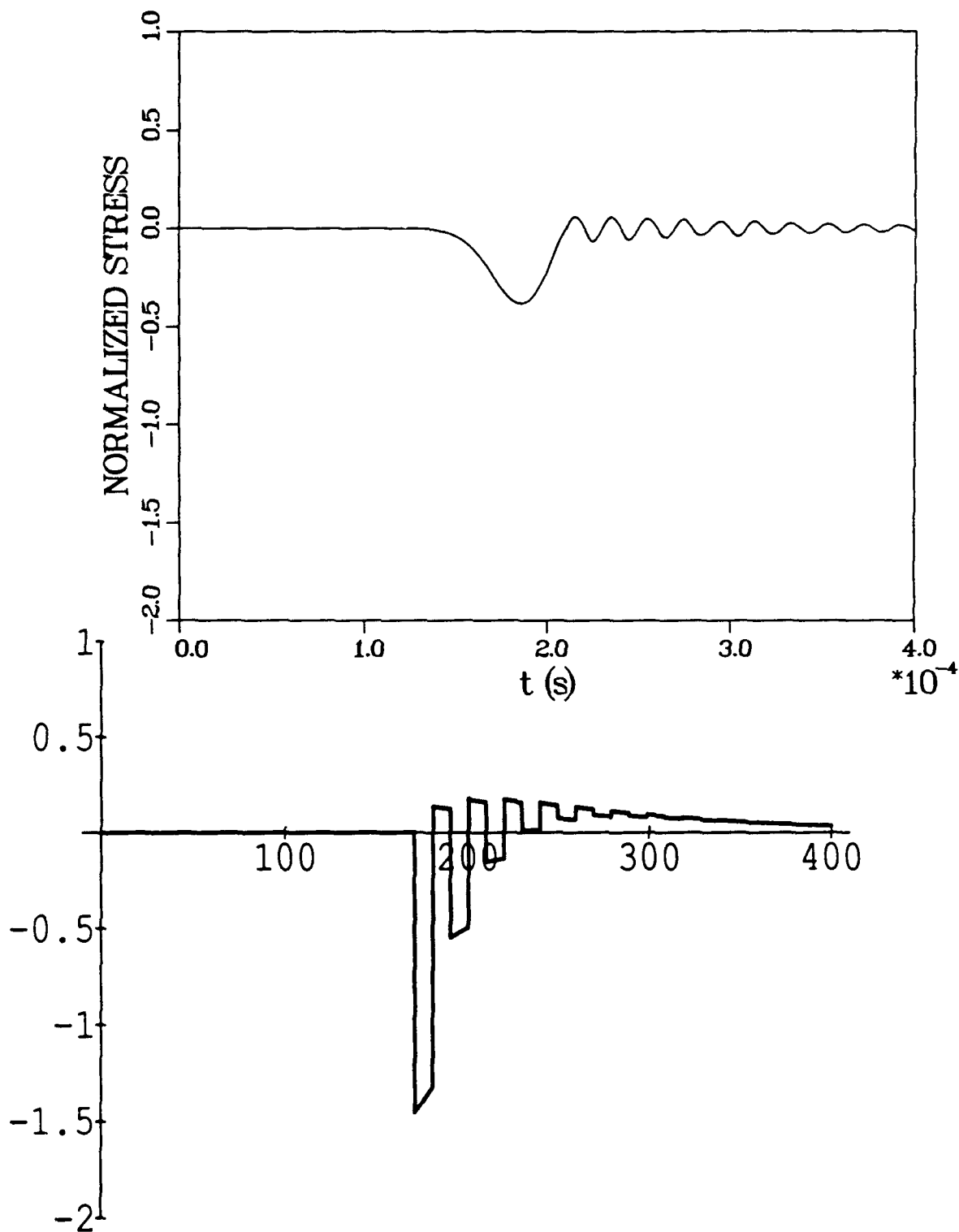


Figure 7.5 Finite-element and analytical results for σ_{zz} at midthickness of the graphite/epoxy plate subjected to plane shock wave loading.

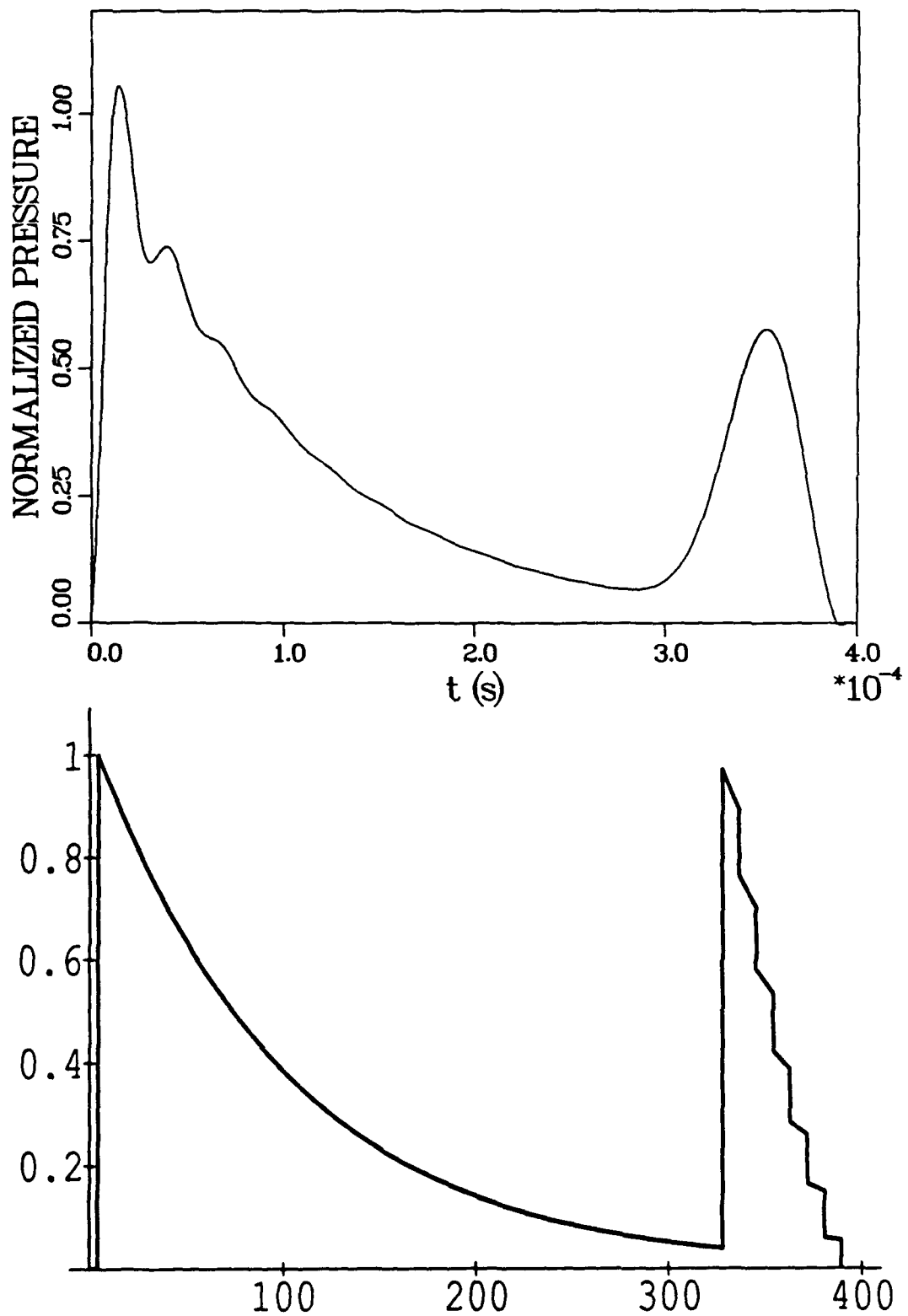


Figure 7.6 Finite-element and analytical results for pressure at the boundary of the fluid due to plane shock wave loading on a steel plate.

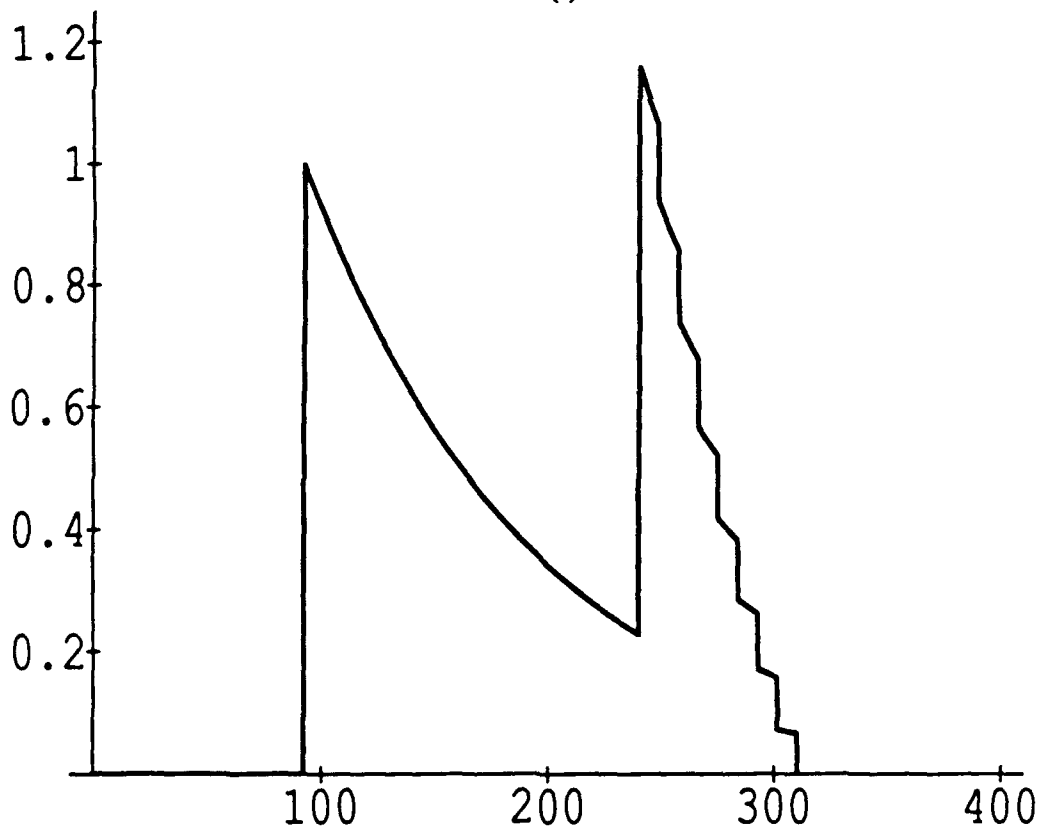
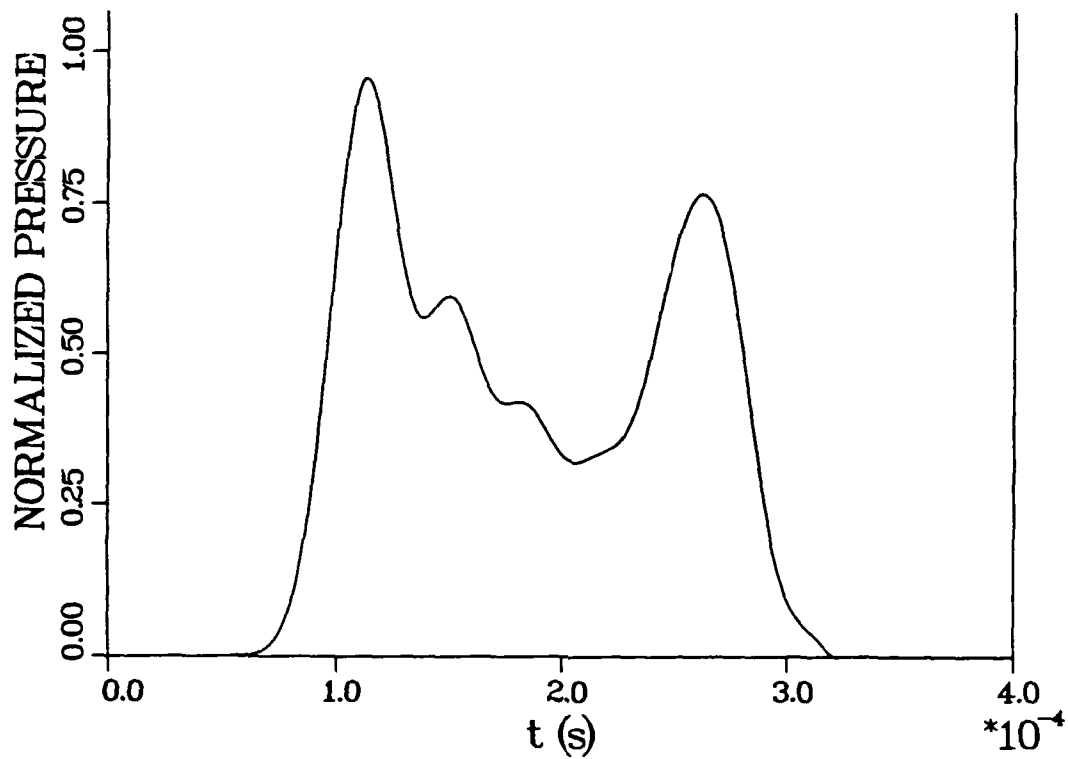


Figure 7.7 Finite-element and analytical results for pressure in the fluid at $z = -113$ mm due to plane shock wave loading on a steel plate.

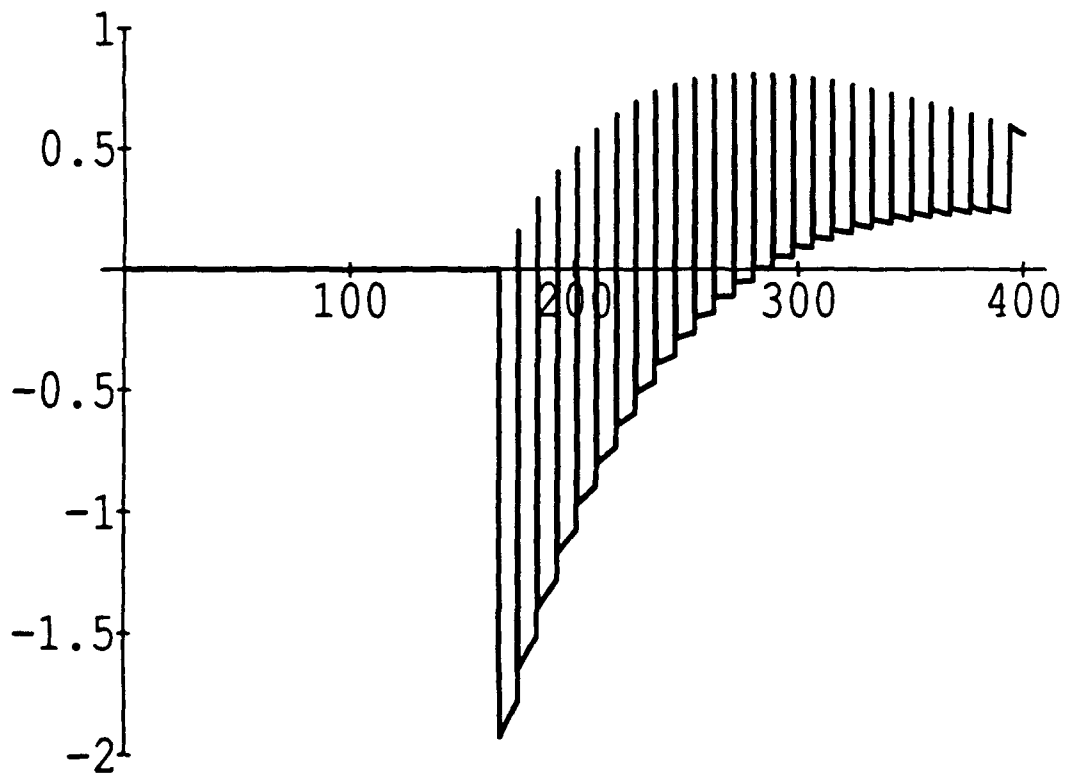
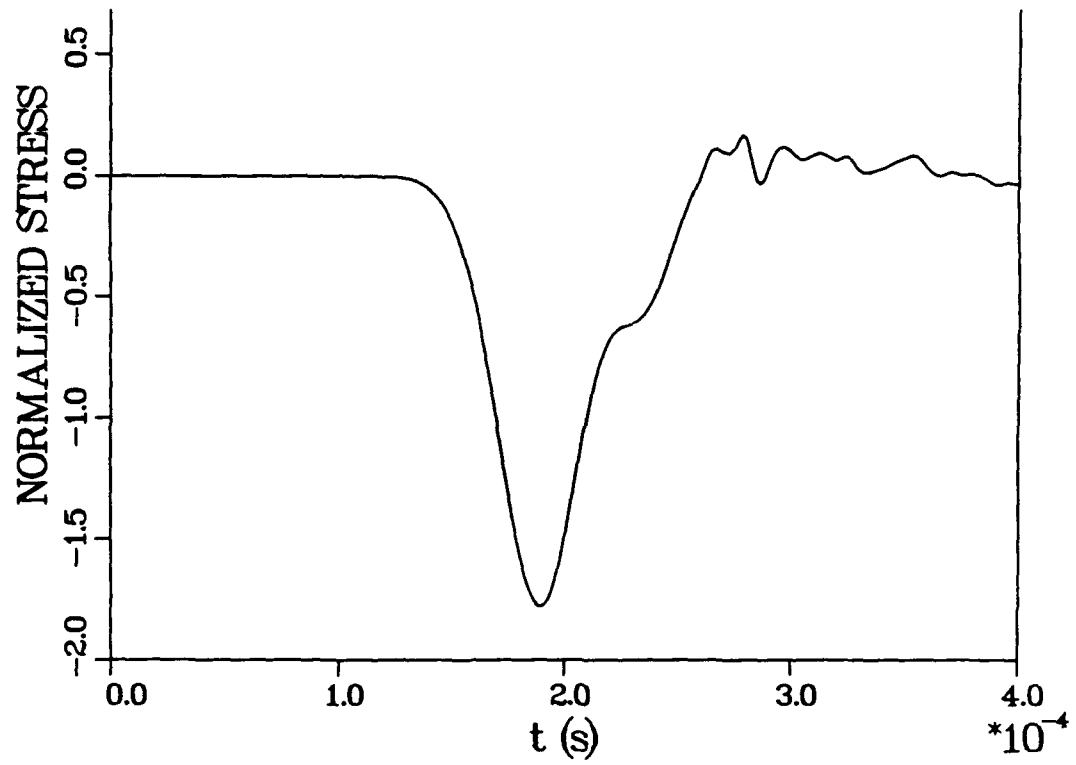


Figure 7.8 Finite-element and analytical results for σ_{zz} near the solid-fluid interface for the steel plate subjected to plane shock wave loading.

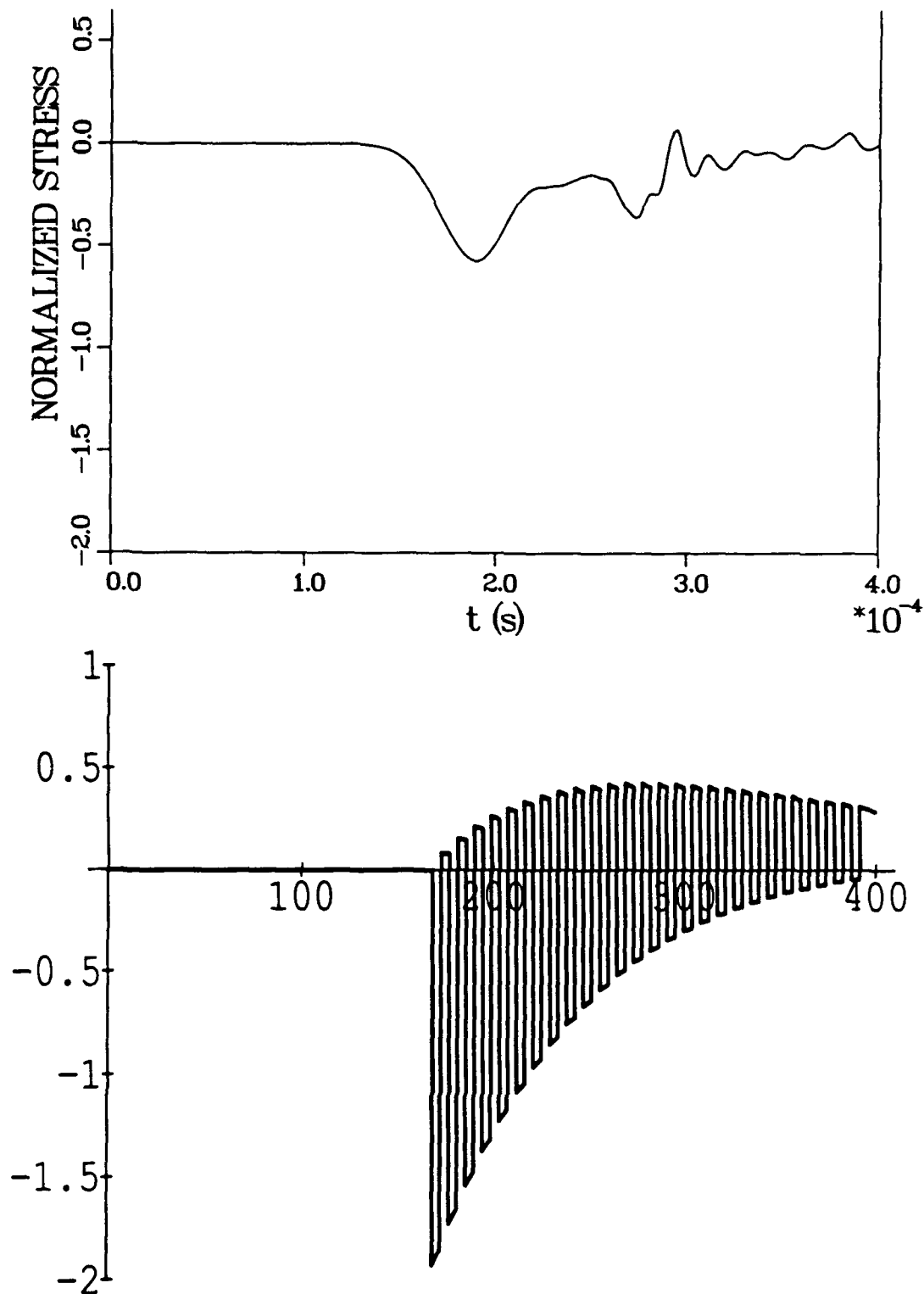


Figure 7.9 Finite-element and analytical results for σ_{zz} at midthickness of the steel plate subjected to plane shock wave loading.

graphite/epoxy plates due to the higher wave speed in the steel. The spread out shock front that occurs in the fluid travels faster through the steel than in the graphite/epoxy. Thus the reflected wave from the free rear surface of the plate has already reached the midplane before the spread out compressive wave has been able to reach its peak value as shown in Figure 7.9.

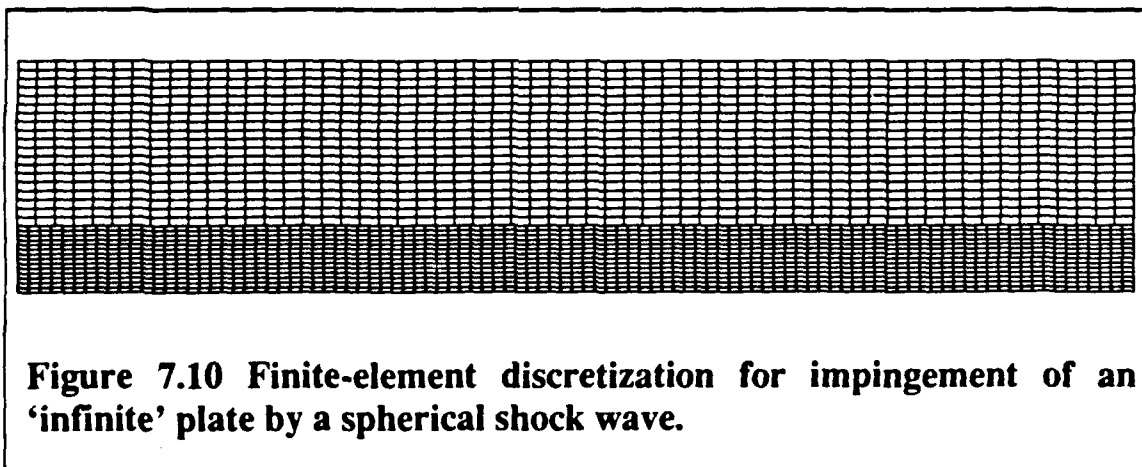
The results of the comparisons show that the finite-element analysis correctly predicts the trends seen in the analytical solution. However because of the coarse discretization employed in the modelling, spreading of the shock wave occurs which results in under predicted stresses in the plate, which in some cases is quite significant. It should be noted here, however, that the analytic solution is based on a linear, elastic, homogeneous solid. Therefore its application to wave propagation in heterogeneous media cannot account for dispersion that occurs as a result of differences in the material behavior of the two phases. In fact the dispersion that takes place in the real composite material is somewhat similar to the numerical dispersion that occurs as a result of the artificial viscosity and discretization used in the analysis as discussed in Section VI. Because of this similarity a viscosity term similar to artificial viscosity is sometimes employed to mimic the dispersion seen in these materials [26]. It appears that a finer discretization of the fluid will be required to prevent spreading of the shock front, particularly when the stresses in the through thickness direction are of interest. In subsequent computations a discretization of the fluid is used having a dimension in the z-direction that is one fourth that used here.

Spherical Wave on an Infinite Plate

The second problem considered is for a spherical wave impinging on an infinite plate. The temporal distribution of the wave is that given by Equation

(5.2). The simulation is conducted for steel since analytical results are available for only isotropic materials. A 25.4 mm thick plate is considered and the center of the spherical wave is taken as $R=0$ and $Z=-257$ mm. The analytical solution is given by Huang [27], and utilizes the Mindlin [28] plate equations of motion including rotatory inertia and transverse shear terms. The plate theory considers the normal stress in the z -direction to be zero, which differs from the finite-element modelling using the two dimensional uniform strain quadrilaterals, which also permits higher order shear-deformation through the overall thickness than the Mindlin theory. Nevertheless, the comparison of the finite-element solution to that given by the analytic solution is valuable to determine the ability of the modelling procedure to predict plate response, which is predominately flexural behavior. This represents the extreme from the problem considered in the preceding subsection, in which no flexural behavior existed and the response was dominated by through thickness wave propagation.

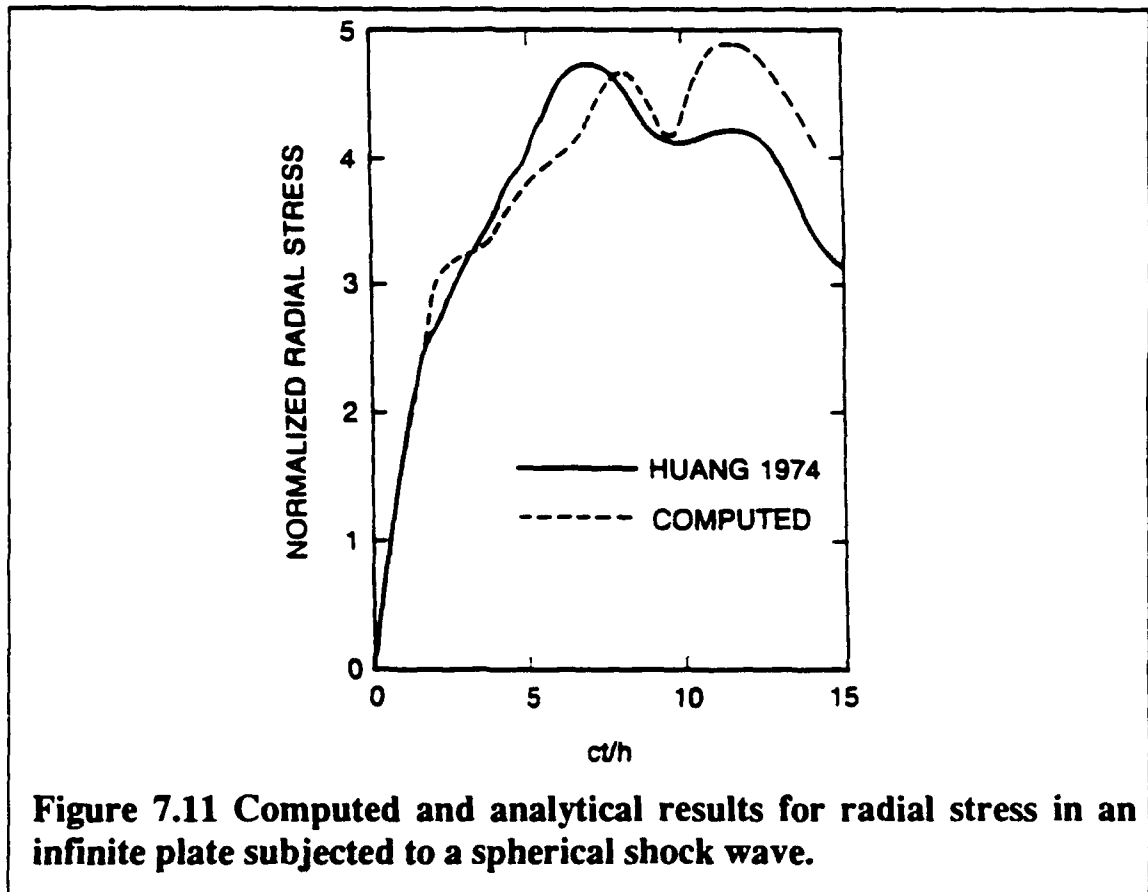
The finite-element model for this problem is shown in Figure 7.10. Radially



the problem is modelled out to $R = 420$ mm. Thus the model can be used to represent an 'infinite plate' only until such time that disturbances can propagate to the outer boundary of the plate and back to the point of interest. Using the wave velocity computed from Equation (7.4) for steel, this results

in a time of 0.1448 msec for the center of the plate ($R=0$). The portion of the fluid modelled extends to $Z = -63.5$ mm and uses a mesh of 19×59 elements. The solid uses a mesh of 14×99 elements.

Results are given in terms of radial stress at the back surface of the plate normalized by the peak pressure P_m of the incoming spherical wave. The history is given in terms of normalized time, $\tau = ct/h$, where c is the wave speed in the fluid, t is time after the wave impinges on the plate, and h is the plate thickness. The finite-element solution is valid for an infinite plate up to $\tau = 17.4$. The computed and analytical results are shown in Figure 7.11. The



comparison shows good overall agreement, particularly with respect to the peak radial stress reached. Discrepancies are expected since the finite-element solution contains through-thickness stress and the analytical solution does not.

Simply Supported Plate

In this subsection the response of a simply supported plate to a spherical shock wave is considered. Plates of 25.4 mm and 50.8 mm thicknesses using properties for both steel and graphite/epoxy are considered in the simulations. The plates are restrained in the z-direction at the outer three node points along the upper and lower surface of the plates. This results in an effective plate diameter of 267 mm. The finite element discretization for the 25.4 mm thick plate and the 50.8 mm thick plate are shown in Figure 7.12 and Figure 7.13,

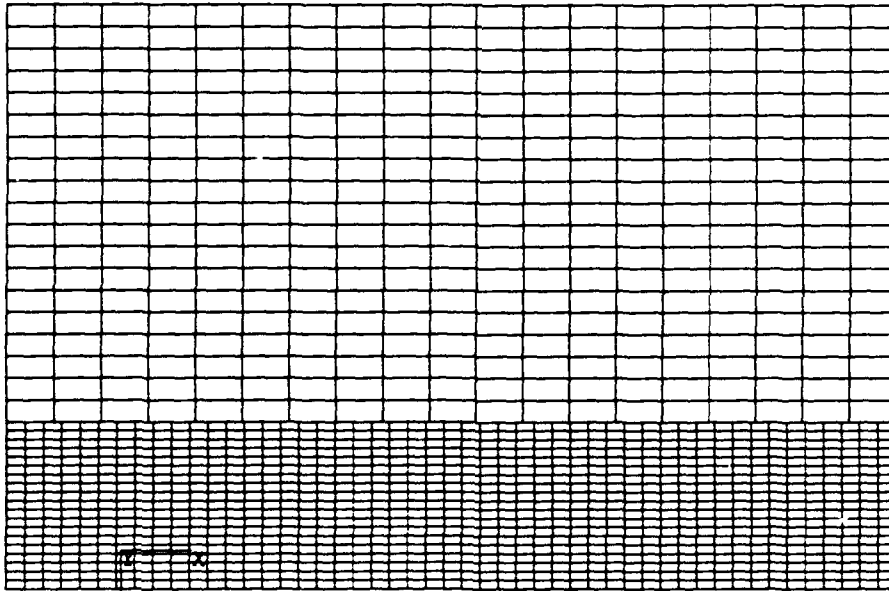


Figure 7.12 Finite-element discretization for impingement of a spherical shock wave on a 25.4 mm thick plate.

respectively. The origin of the spherical wave is at $R=0$, $Z=-245$ mm.

Of interest in these simulations is both the early time response as well as the late time response. Early time response, is taken here to be that part of the response which is governed by wave propagation in the through-thickness direction of the plate. The through-thickness stresses are responsible for spallation or delamination type damage in composite plates. For the 25.4 mm

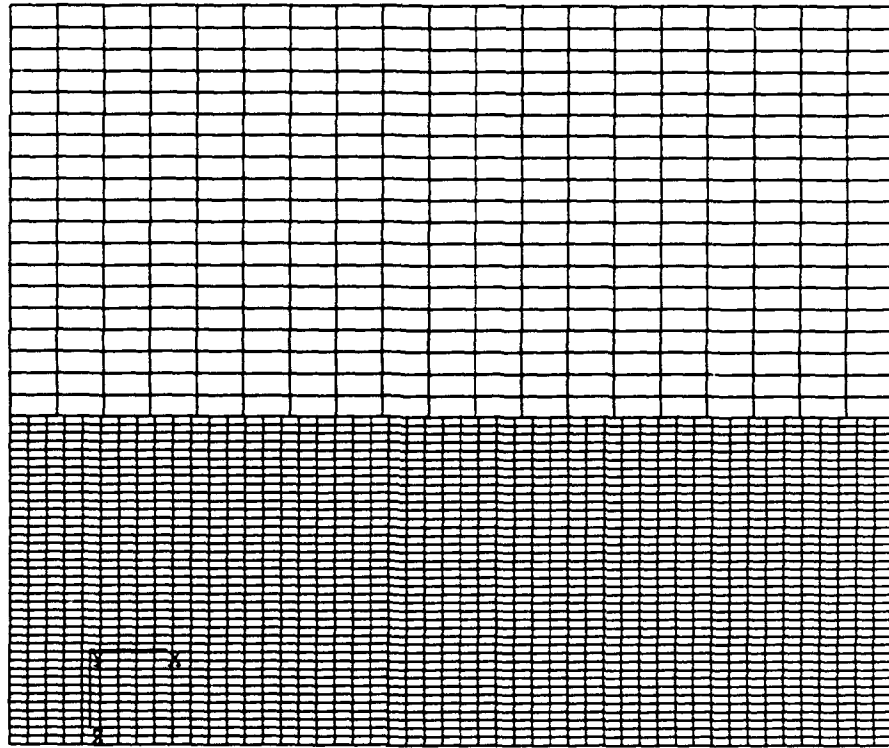


Figure 7.13 Finite-element discretization for impingement of a spherical shock wave on a 50.8 mm thick plate.

this early time is on the order of 50 -100 μ sec. The late time-response is that portion of the response dominated by overall flexure of the plate. It is this portion of the response that results in matrix cracking, fiber breakage and overall flexural collapse under sufficient loading. Late-time response can be estimated by considering the fundamental frequency of the plate with coupled fluid mass. For the configuration considered here the late-time response occurs in the range of 0.1-1.0 msec.

For the early time response of the 25.4 mm plate, the stress history at two elements within the plate will be investigated. The first of these is at $R=1.71$ mm and $Z=0.668$ mm, which essentially gives the stress transmitted to the plate directly below the origin of the spherical loading. The normalized stress history for both the graphite/epoxy plate and that for a steel plate is given in

Figure 7.14. As seen in the previous subsection, the stress wave transmitted to

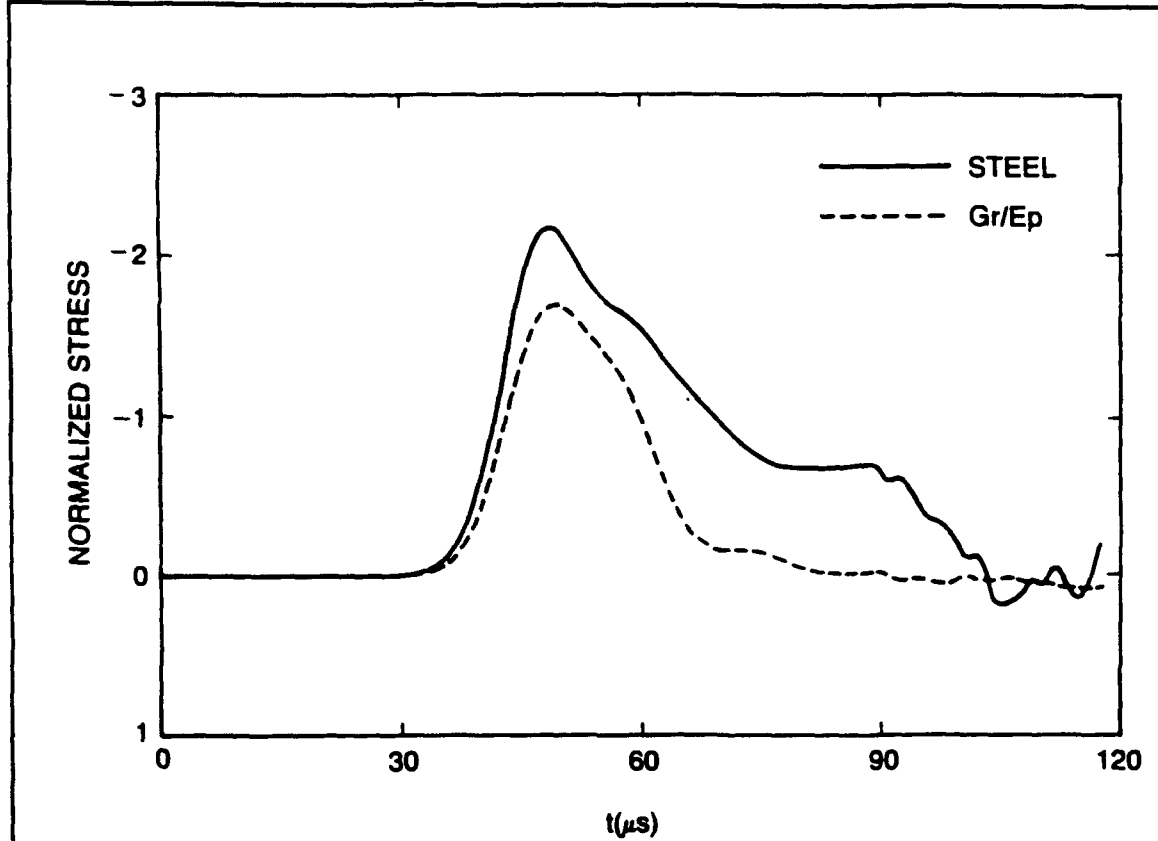


Figure 7.14 Normalized stress σ_{zz} near the solid-fluid interface in 25.4 mm thick graphite/epoxy and steel plates subjected to a spherical shock wave.

the steel plate is significantly higher than that transmitted to the graphite/epoxy plate. An integration of the stress history over time is a measure of the momentum density at that location. The z-component of momentum density, M_z , is given by

$$M_z = \int_0^t (\sigma_{zr} n_r + \sigma_{zz} n_z) dt \quad (7.5)$$

where n_r and n_z are the components of the unit normal vector in the radial and through thickness direction, respectively. Considering the stress state at the surface of the plate, the shear stress is zero and the outer normal is along the z-direction so that Equation (7.5) reduces to the integration of the normal stress history in the z-direction over time, which is shown in Figure 7.14.

Performing the integration, the momentum density transferred to the graphite/epoxy is approximately 50% of that transferred to the steel. The reduced amount of momentum density transferred to the plate is significant since the total momentum must be resisted by stresses within the plate during the flexural deformation.

The through thickness stress (σ_{zz}) is also shown for an element that is at the plate mid-thickness. The stress history for both the steel and graphite/epoxy plates are shown in Figure 7.15. Of interest here is that, because of the slower

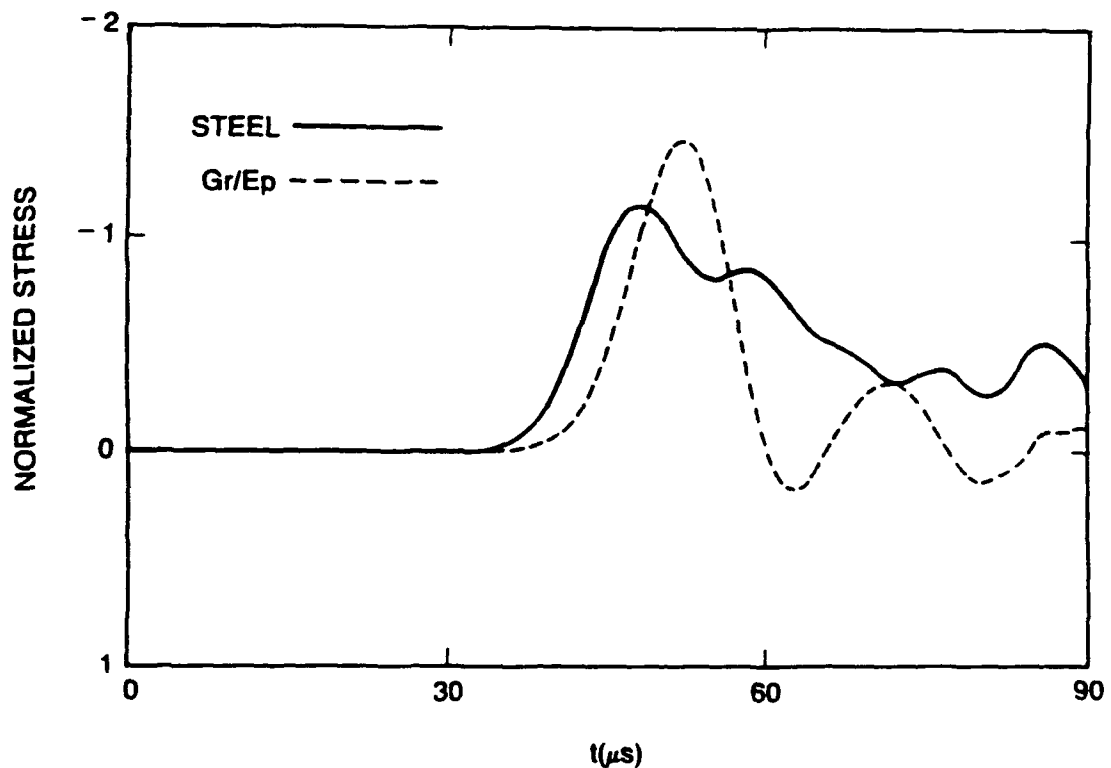


Figure 7.15 Normalized stress σ_{zz} at the midplane of 25.4 mm thick graphite/epoxy and steel plates subjected to a spherical shock wave.

wave speed in the thickness direction, the graphite/epoxy plate develops tensile stresses after the reflection of the wave from the rear surface.

The late time response is manifested by the flexural deformation of the plate.

Figure 7.16 show the deformed geometry of the plate at several instants of

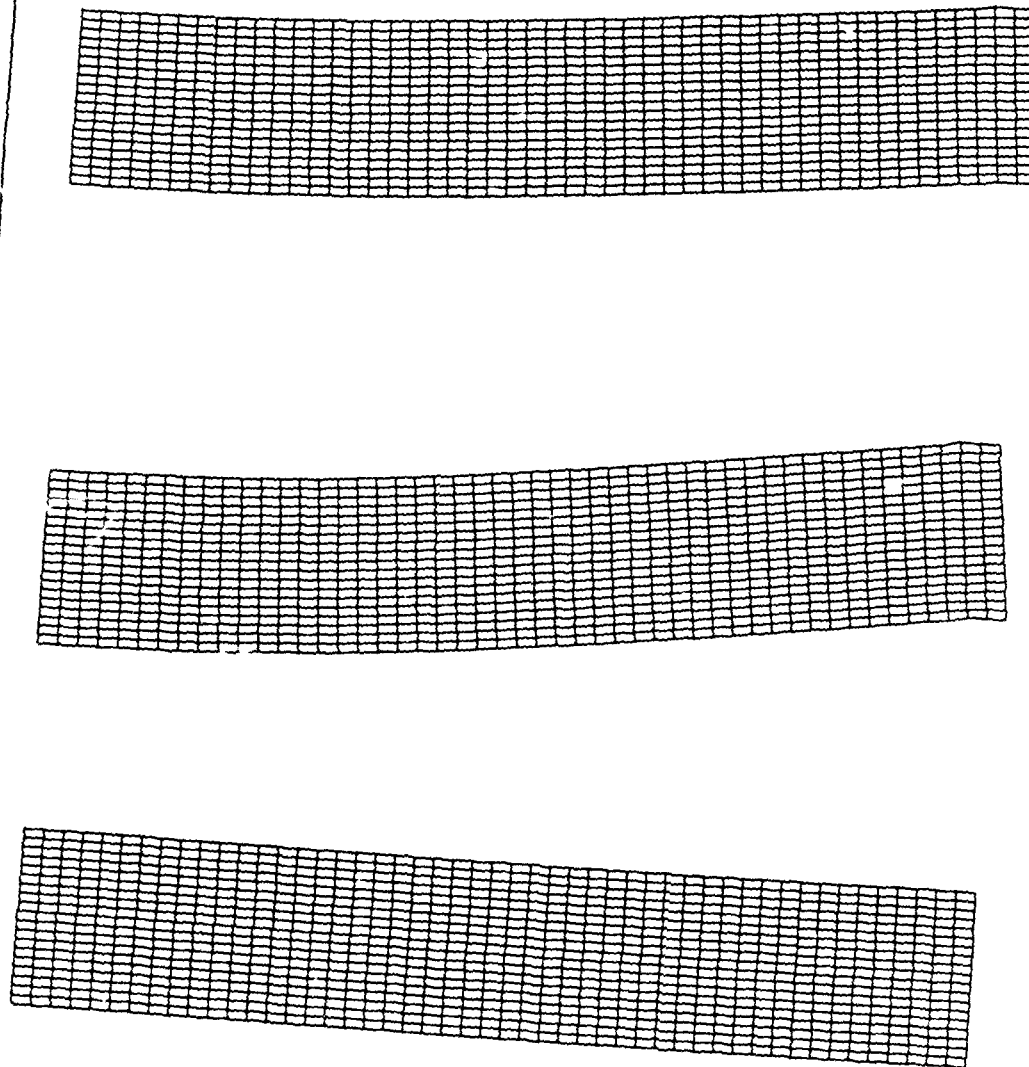
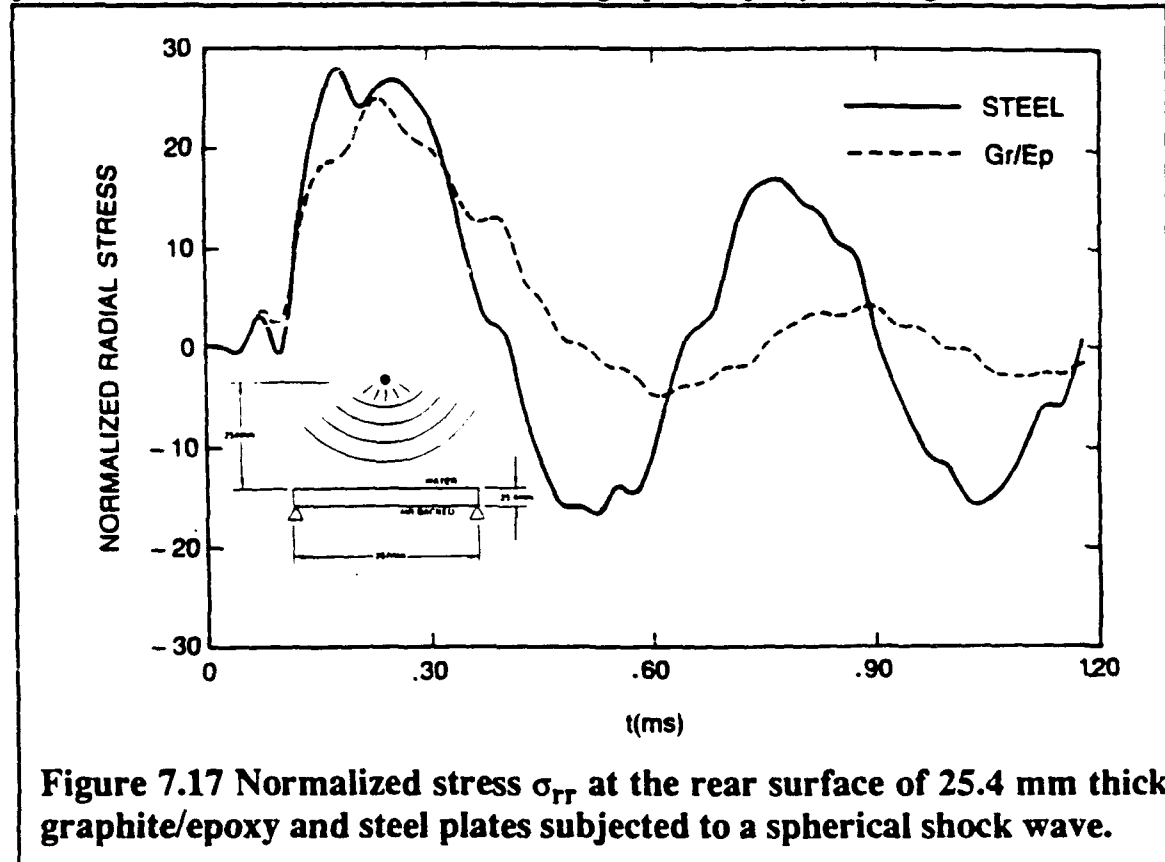


Figure 7.16 Deformed geometry of the 25.4 mm thick graphite/epoxy plate subjected to a spherical shock wave at 150, 250, and 500 μ sec.

time. As can be seen the plate deforms essentially in a fundamental mode of vibration. The boundary conditions at the edge of the plate simulate a simply supported restraint as rotation of the midplane is evident. The restraint of just three node points along top and bottom surfaces does however result in very

high local stresses in the region of the restraint. In simulation of the EBT it would be preferable to use a contact surface support over the length of plate that is actually restrained. The radial stress history at the rear surface of the plate is shown for both steel and graphite/epoxy in Figure 7.17. The



alternating tensile and compressive stresses at the point again shows that the plate is vibrating in essentially its fundamental mode. The maximum stress level reached is slightly higher in the steel. Maximum elastic deflection in the graphite/epoxy plate is 2.79 times that in the steel, but of course, the weight of the steel is 5 times that of the graphite/epoxy.

The response of the 50.8 mm thick graphite/epoxy plate is considered next. The plate has the same boundary conditions and is subjected to the same loading as the 25.4 mm thick plate. The normal stress at the plate surface is shown in Figure 7.18. Comparing the pulse to that shown in Figure 7.13 for the 25.4 mm graphite/epoxy plate shows it to be longer due to the longer time

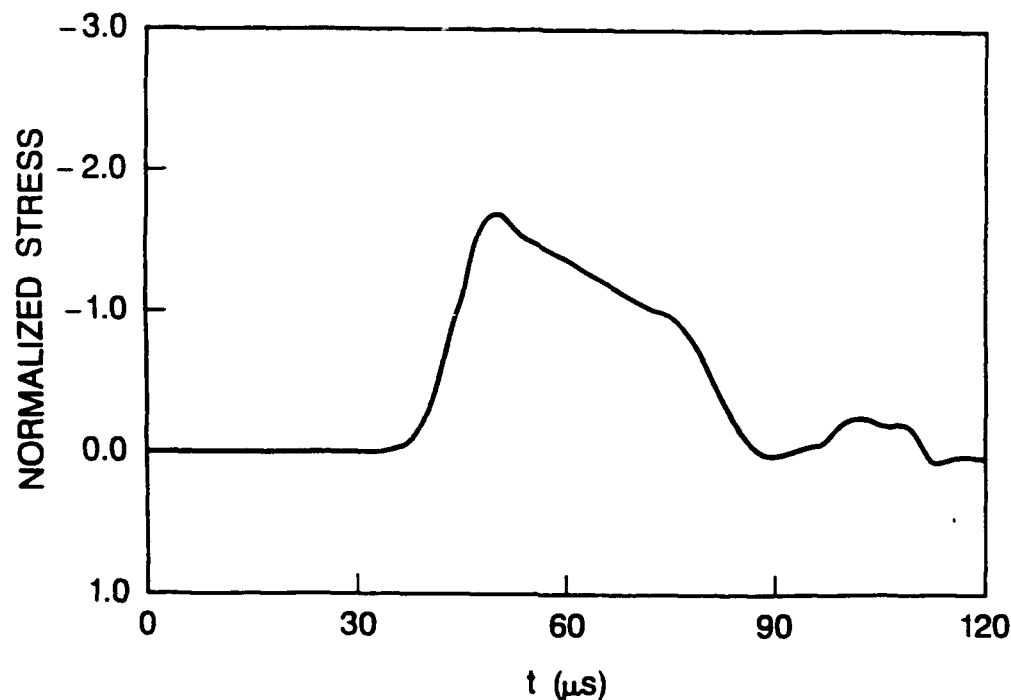
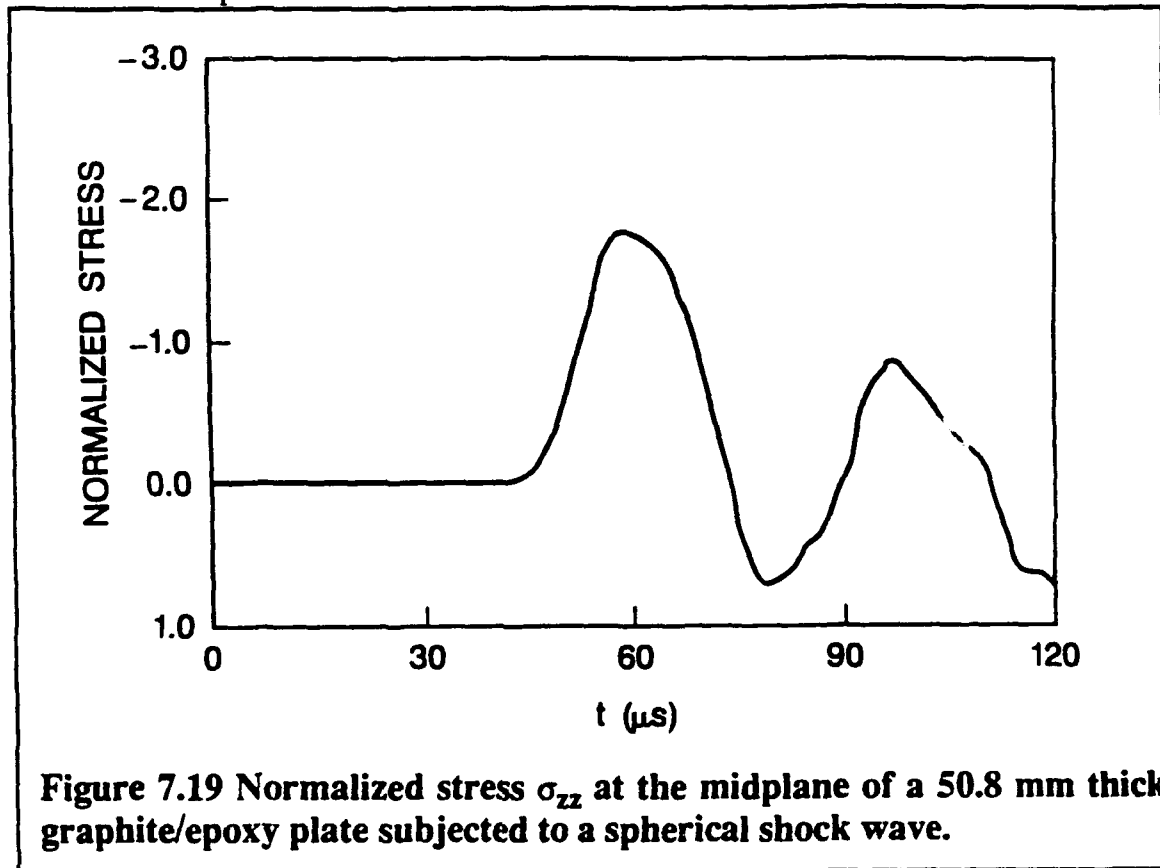


Figure 7.18 Normalized stress σ_{zz} at the solid-fluid interface of a 50.8 mm thick graphite/epoxy plate subjected to a spherical shock wave.

for the wave to travel to the rear surface and back to the front. The normal stress at the mid-plane of the plate thickness is shown in Figure 7.19. Of particular importance is that now the tensile stresses that develop are significantly larger than those that develop in the 25.4 mm thick plate, and are approximately 0.75 times the magnitude of the incoming wave. Thus for thicknesses larger than 50.8 mm, tensile stresses approaching the magnitude of the incoming wave would be expected. The late time response of the 50.8 mm plate is illustrated through the sequence of deformed geometry plots shown in Figure 7.20. The maximum deflection in the 50.8 mm graphite/epoxy plate is 0.358 times that of the 25.4 mm graphite/epoxy plate or approximately the same as that of the 25.4 mm steel plate. The radial stress history at the center of the rear surface of the plate is shown in Figure 7.21.

Comparison with Figure 7.17 shows the maximum stresses to be one-half that of the thinner plate.



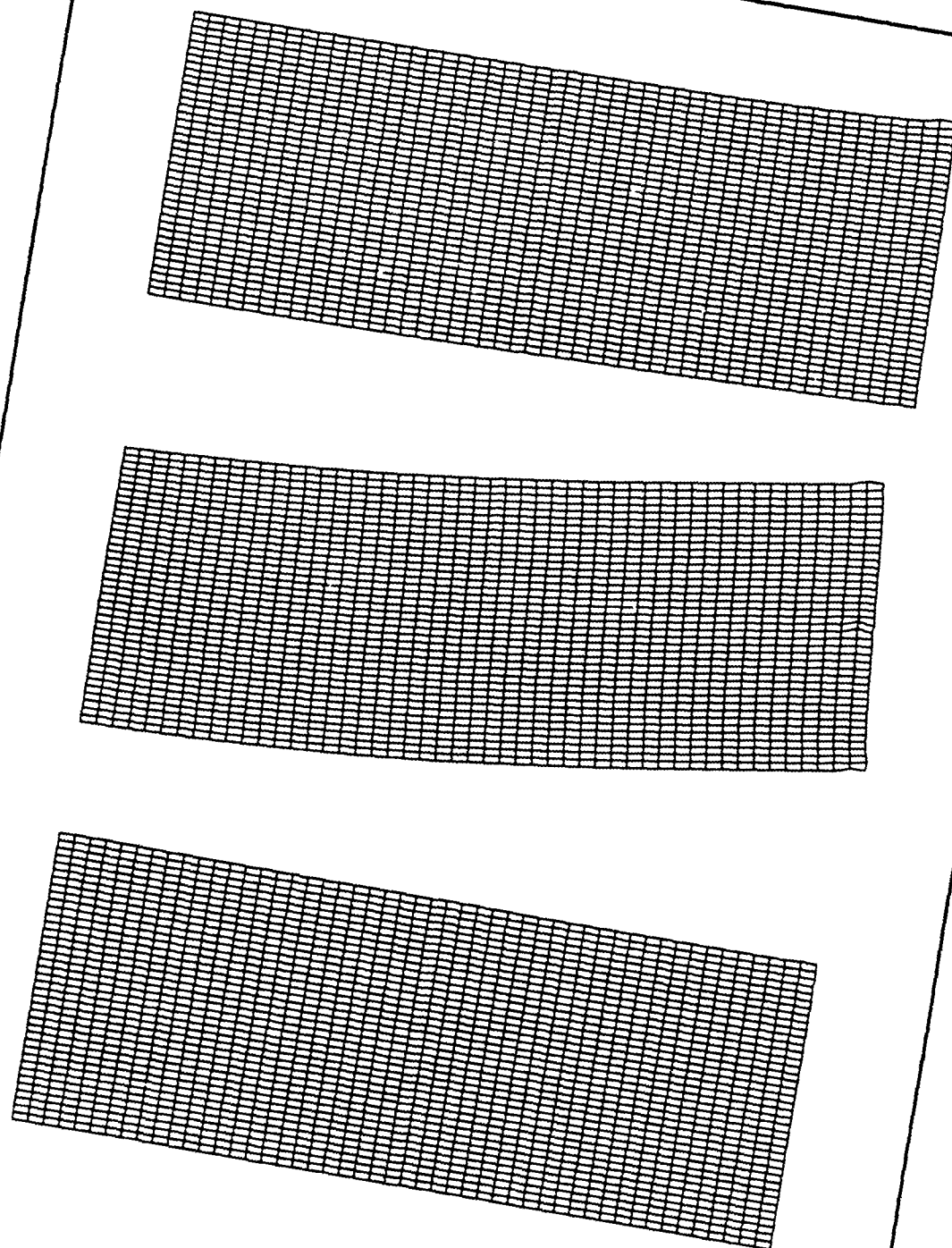


Figure 7.20 Deformed geometry of the 50.8 mm thick graphite/epoxy plate subjected to a spherical shock wave at 75, 175, and 300 μ sec.

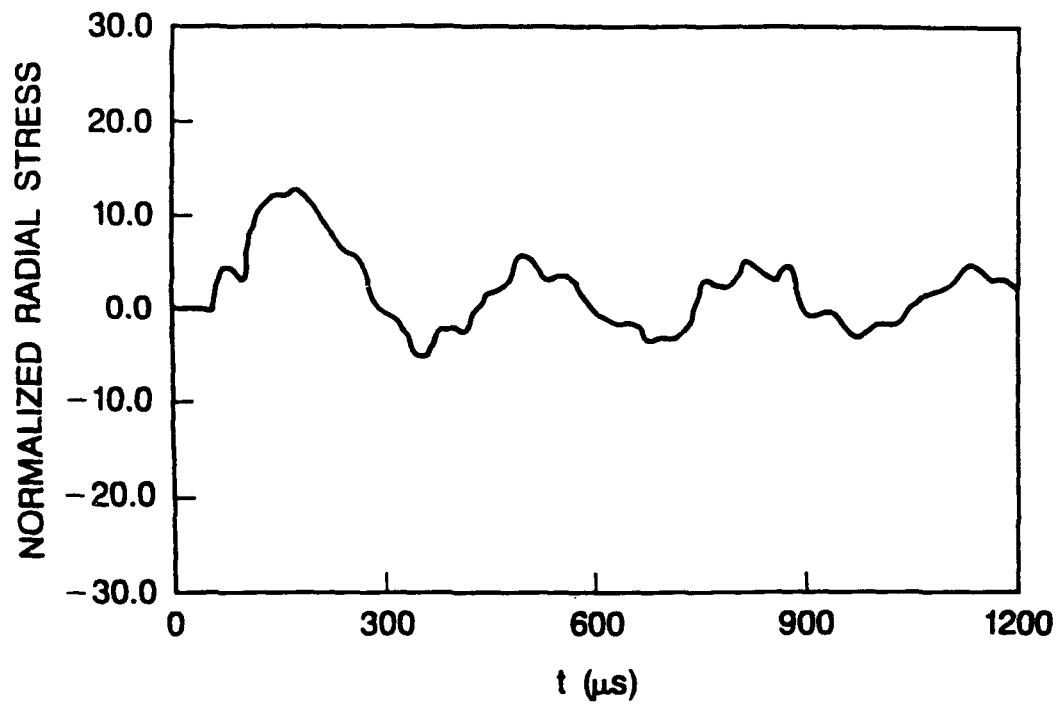


Figure 7.21 Normalized stress σ_{rr} at the rear surface of a 50.8 mm graphite/epoxy plate subjected to spherical shock wave.

VIII. DEVELOPMENT OF THE DAMAGE MODEL

A continuum damage model (CDM) is developed to simulate the onset of damage and the subsequent softening effects of various degradation mechanisms. This capability will be useful to design tests, to analyze test data, and to simulate various operating or threat conditions. There is a fairly large literature in CDM and some of that work is followed in the development given here. In particular, the works of Davison and Stevens [29], Krajcinovic [30], and Talreja [31], with appropriate simplifications and extensions, are used for guidance.

A distributed or continuous damage model is particularly appropriate for composite materials because of their tendency to arrest propagating flaws, soften and redistribute the loads. At high loading rates, even delamination phenomena, which might behave as single fracture planes on slow loading, tend to disperse into a distributed pattern of small cracks which cannot run as fast as the loading process progresses and which may be amenable to modeling by a CDM approach. The model described here is linear in strain, but nonlinear in damage due to softening effects.

Material Description

This damage model is restricted to a thick laminated composite material, a portion of which is shown in Figure 8.1, with no fiber reinforcement in the 1-direction (through-thickness and generally the wave propagation direction) and a balanced (isotropic) arrangement of reinforcing fibers in the 2,3-plane (in-plane). The material is assumed to be exactly transversely isotropic with respect to both stiffnesses and developing damage with the 2,3-plane being the plane of isotropy. This material symmetry is attained approximately by the usual filament wound or flat layup composites with balanced 0° , $\pm 60^\circ$ (as in Figure 8.1) or 0° , 90° , $\pm 45^\circ$ layups. The approximation of transverse isotropy

is, of course, much better for stiffnesses, but is also imposed on damage development in this treatment.

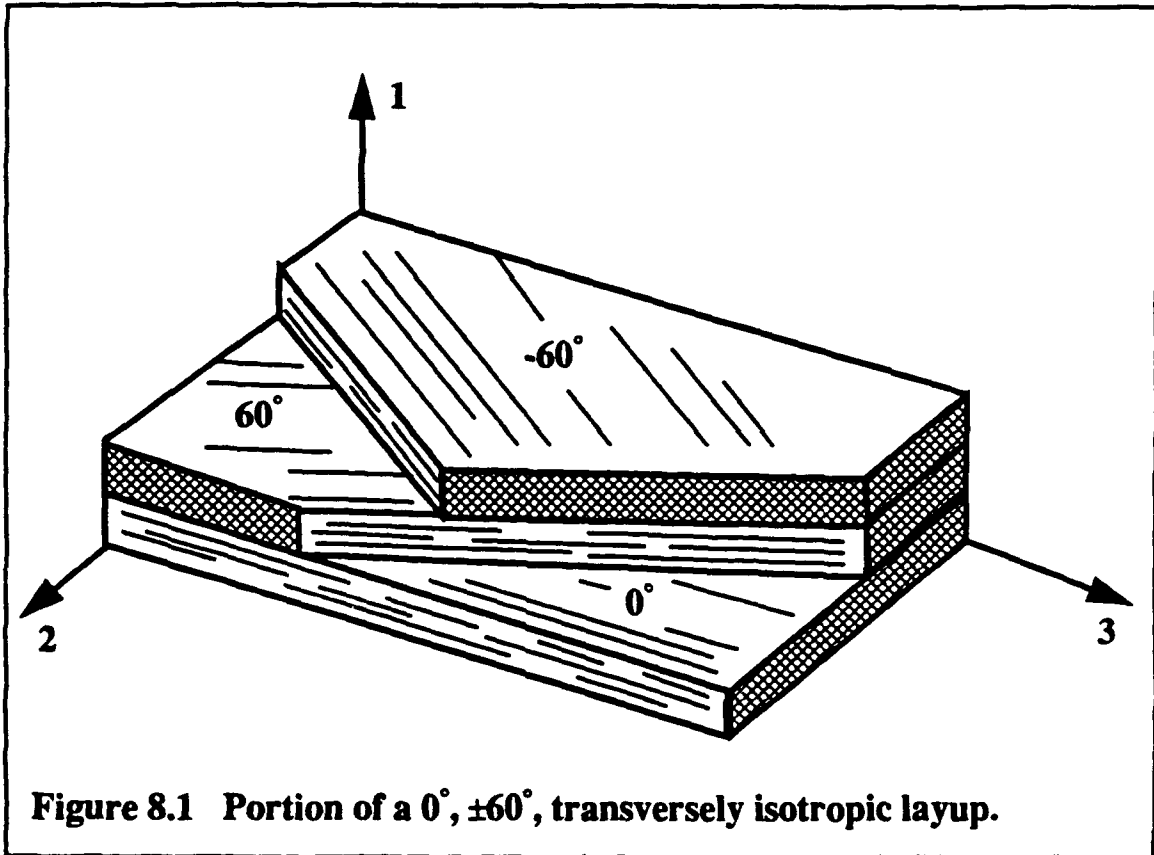
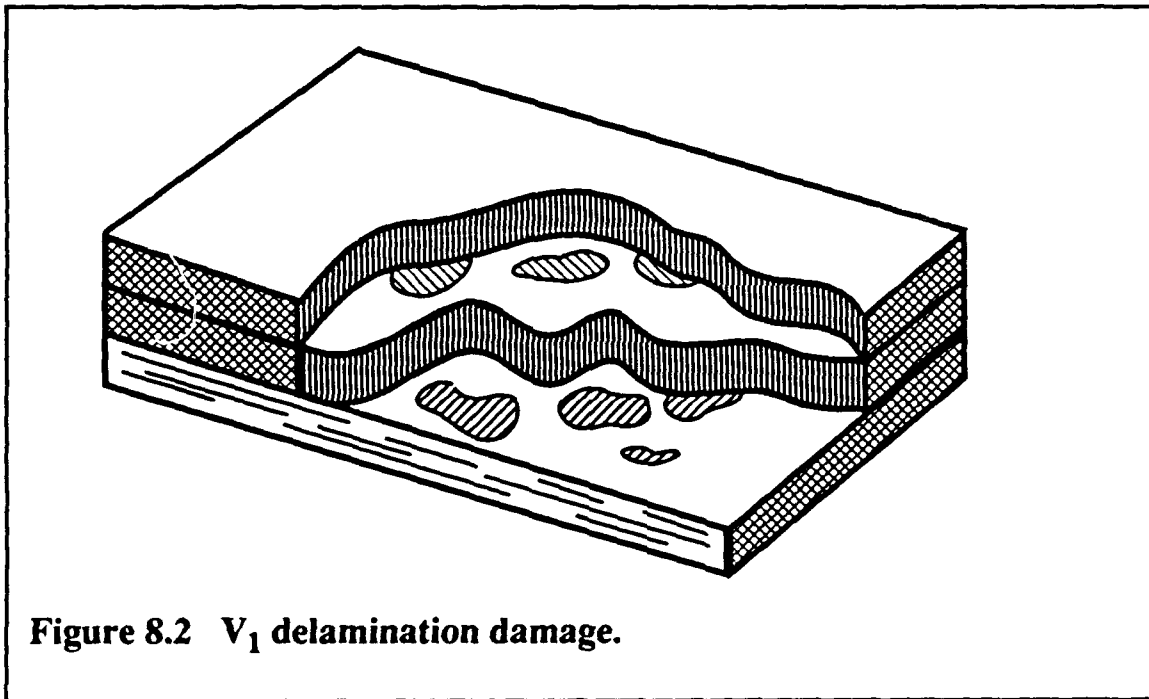


Figure 8.1 Portion of a $0^\circ, \pm 60^\circ$, transversely isotropic layup.

Damage Description

The evolving modes of damage are restricted to certain orientations of brittle cracking of the matrix material. A simple maximum strain criterion is used for fiber breakage with no allowance for evolution. The matrix damage is characterized by the vector $\bar{V}=(V_1, V_2, V_3)$ referred to the material coordinate system shown in Figure 8.1 with the indices denoting direction of the prevailing normal to the plane of the cracks and the magnitudes denoting a measure of the severity of the damage. This severity might take the form of a normalized local areal density of crack surfaces. However, in the present phenomenological treatment, damage magnitude is interpreted simply in terms of fractional reduction of certain elastic properties of the material.

The V_1 component of damage is intended to represent a network of matrix cracking predominately aligned in the 2,3-plane (with normals in the 1-direction) which do not cross reinforcing fibers and which lead ultimately to delamination failure. It is intended that V_1 damage will describe spallation damage due to through-thickness waves and the progression of damage leading to complete separation due to spallation. A state of V_1 damage is shown schematically in Figure 8.2.



The remaining matrix damage is characterized by a combination of V_2 and V_3 damage. This is due to matrix cracks which may traverse or lie between reinforcing fibers, but which do not break the fibers. This damage is assumed to occur in a randomly distributed fashion both spatially and by orientation (by combinations of V_2 and V_3) of normals in the 2,3-plane such that the degraded material properties are left transversely isotropic. Such will be the case if the average degradation is independent of the orientation of the V_2 , V_3 components of the damage vector. This is assumed to be the case and, further, that the material property degradation depends only on the magnitude

$$V_S = \sqrt{V_2^2 + V_3^2} \quad (8.1)$$

of the in-plane components of the damage vector. Thus, the in-plane damage V_S is characterized by a scalar with indefinite direction, except that it is oriented perpendicular to the V_1 component of damage. The V_1 and V_S damages are contrasted also with regard to their evolution to very different end states. Whereas the V_1 damage evolves, perhaps catastrophically, to a delamination or spallation with complete separation, the V_S damage evolves to a spatially saturated state of damage defined by $V_S=1$ and is followed by other modes of damage (either fiber breakage or further delamination damage). The V_S damage is shown schematically in Figure 8.3.

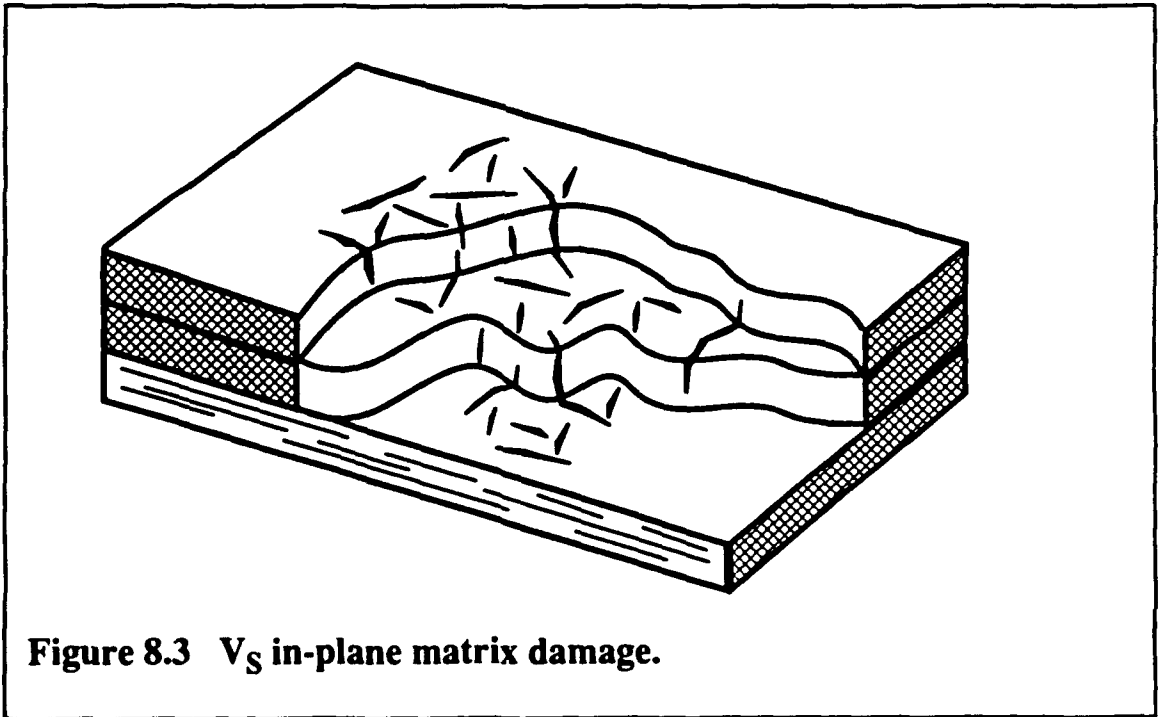


Figure 8.3 V_S in-plane matrix damage.

Material Model

Talreja's [31] development for vector damage in a transversely isotropic material is followed here. The assumption of small damage is relaxed since the full evolution of damage to an end state is sought. The material response is further restricted to axisymmetry with the 1-axis being the axis of symmetry

and with the 2- and 3-directions now being identified with r (radial) and θ (circumferential) cylindrical coordinates. Placing small strain and reflection symmetry requirements (independent of sign of V_1 and V_S) on \bar{V} , leads to a Helmholtz free energy function

$$\rho\psi = f(I_1, I_2, \dots, I_6) \quad (8.2)$$

of the strain and damage invariants

$$\begin{aligned} I_1 &= \epsilon_{11} \\ I_2 &= \epsilon_{22} + \epsilon_{33} \\ I_3 &= \epsilon_{22}^2 + \epsilon_{33}^2 \\ I_4 &= \epsilon_{12}^2 \\ I_5 &= V_1^2 \\ I_6 &= V_S^2 = V_2^2 + V_3^2. \end{aligned} \quad (8.3)$$

The stress tensor components result from the derivatives $\sigma_{ij} = \partial(\rho\psi) / \partial \epsilon_{ij}$ and are expressed in the usual transversely isotropic, axisymmetric, linear constitutive form as

$$\begin{bmatrix} \sigma_{11} \\ \sigma_{22} \\ \sigma_{33} \\ \sigma_{12} \end{bmatrix} = \begin{bmatrix} C_{11} & C_{12} & C_{12} & 0 \\ C_{12} & C_{22} & C_{23} & 0 \\ C_{12} & C_{23} & C_{22} & 0 \\ 0 & 0 & 0 & C_{44} \end{bmatrix} \begin{bmatrix} \epsilon_{11} \\ \epsilon_{22} \\ \epsilon_{33} \\ \epsilon_{12} \end{bmatrix} \quad (8.4)$$

where the elastic coefficients C_{ij} are functions of the damage invariants $I_5 = V_1^2$ and $I_6 = V_S^2$. To facilitate simple assumptions on damage dependence, (8.4) is inverted to the following compliance form

$$\begin{bmatrix} \epsilon_{11} \\ \epsilon_{22} \\ \epsilon_{33} \\ \epsilon_{12} \end{bmatrix} = \begin{bmatrix} 1/E_{11} & -\nu_{12}/E_{11} & -\nu_{12}/E_{11} & 0 \\ -\nu_{12}/E_{11} & 1/E_{22} & -\nu_{23}/E_{22} & 0 \\ -\nu_{12}/E_{11} & -\nu_{23}/E_{22} & 1/E_{22} & 0 \\ 0 & 0 & 0 & 1/(2G_{12}) \end{bmatrix} \begin{bmatrix} \sigma_{11} \\ \sigma_{22} \\ \sigma_{33} \\ \sigma_{12} \end{bmatrix} \quad (8.5)$$

where

$$\begin{aligned}
C_{11} &= \frac{(1 - \nu_{23}) E_{11}}{1 - \nu_{23} - (2\nu_{12}^2 E_{22}) / E_{11}} \\
C_{22} &= \frac{[1 - (\nu_{12}^2 E_{22}) / E_{11}] E_{22}}{(1 + \nu_{23}) [1 - \nu_{23} - (2\nu_{12}^2 E_{22}) / E_{11}]} \\
C_{12} &= \frac{\nu_{12} E_{22}}{1 - \nu_{23} - (2\nu_{12}^2 E_{22}) / E_{11}} \\
C_{23} &= \frac{[\nu_{23} - (\nu_{12}^2 E_{22}) / E_{11}] E_{22}}{(1 + \nu_{23}) [1 - \nu_{23} - (2\nu_{12}^2 E_{22}) / E_{11}]} \\
C_{44} &= 2G_{12} .
\end{aligned} \tag{8.6}$$

The damage dependence is imposed on the compliances in (8.5) since they allow a more intuitive interpretation of damage effect than do the elastic coefficients C_{ij} in (8.4). This can be assumed in a general functional form, to be set by experimental evidence. However, for the sake of demonstrating possible damage effects on constitutive behavior, the following simple damage dependences are assumed:

$$\begin{aligned}
E_{11} &= (1 - V_1^2) E_{11}^0 \\
E_{22} &= (1 - \alpha_1 V_S^2) E_{22}^0 \\
G_{12} &= (1 - V_1^2) (1 - \alpha_2 V_S^2) G_{12}^0 \\
\nu_{12} &= (1 - V_1^2) (1 - \alpha_3 V_S^2) \nu_{12}^0 \\
\nu_{23} &= (1 - \alpha_4 V_S^2) \nu_{23}^0
\end{aligned} \tag{8.7}$$

where the superscript "0" denotes virgin properties and the fractions $0 < \alpha_i < 1$, $i=1,4$ are included to prevent complete loss of material integrity as the saturation state $V_S \rightarrow 1$ is reached. Integrity may remain due to unbroken reinforcing fibers in the 2,3-plane. The particular functional dependence on V_1

and V_S in (8.7) is quite arbitrary except for the fact that the E_{11} and E_{22} dependence can be taken to define V_1 and V_S and, in such case, the remaining functions should be determined by corresponding experimental evidence of material degradation effects on those other material properties. The elastic coefficient dependence on damage is then determined by combining (8.7) with (8.6).

Damage Evolution

Rate dependency (actually, time dependency) is introduced into the CDM process by way of damage evolution with assumed dependence on the current state of damage, some overstress above a current threshold, and material properties controlling evolution rates. There is such a sparsity of data on damage evolution that guidance depends mostly on general intuition and awaits definitive experiments. Curran, et al, [32] give extensive consideration to evolution (growth) and nucleation of voids and Krajcinovic [30], in a review article, addresses the range of possible kinetic laws for damage evolution. The intended application here is to composite materials which usually abound with imperfection sites from which cracks can grow. Thus, nucleation of new cracks is not addressed here and the focus is on growth or evolution of damage.

Both the V_1 and V_S types of damage are assumed to be governed by a threshold of the form

$$\begin{aligned} F(\boldsymbol{\sigma}, \bar{\mathbf{f}}(\bar{\mathbf{V}})) &\leq 0 \text{ for no damage growth} \\ &> 0 \text{ for damage growth} \end{aligned} \tag{8.8}$$

where F is a scalar threshold function, $\boldsymbol{\sigma}$ is the current stress tensor, $\bar{\mathbf{f}}$ is an array of current threshold parameters, which is a function of $\bar{\mathbf{V}}$, the current damage vector. The details of this threshold function are illustrated with the following specific example.

A hyperbolic threshold surface of the Mohr-Coulomb type is taken to be dependent on the stresses σ, τ (tension and shear) as follows:

$$F(\bar{\sigma}, \bar{f}) = \sqrt{1 + (\tau/f_3)^2} - (f_1 - \sigma)/f_2 \quad (8.9)$$

where the parameters \bar{f} are related to specific growth threshold strengths and the Coulomb friction tangent as

$$\begin{aligned} \sigma_G &= f_1 - f_2 \\ \tau_G &= f_3 \sqrt{(f_1/f_2)^2 - 1} \\ \phi_G &= f_3/f_2. \end{aligned} \quad (8.10)$$

These tension and shear growth thresholds and the Coulomb friction tangent in (8.10) are assumed to be functions of the damage V_1 (or V_S). The threshold surface $F=0$ from (8.9) is shown in Figure 8.4 along with parameters and the shortest distance d from an external stress state (σ, τ) to the threshold surface.

For example to complete the threshold specification, the V_1 delamination damage threshold is postulated to depend only on the stress components

$$\begin{aligned} \sigma &= \sigma_{11} \\ \tau &= \sigma_{12}. \end{aligned} \quad (8.11)$$

The growth threshold stress and Coulomb friction tangent in (8.10) are postulated to depend on the damage V_1 as

$$\begin{aligned} \sigma_{G1} &= (1 - V_1^2) \sigma_{G10} \\ \tau_{G1} &= (1 - V_1^2) \tau_{G10} \end{aligned} \quad (8.12)$$

$$\phi_{G1} = \phi_{G10} + V_1^2 (\phi_{G11} - \phi_{G10})$$

where the "0" subscript denotes virgin ($V_1=0$) threshold properties. These simple functions are designed so that all resistance to damage is lost as $V_1 \rightarrow 1$ and so that the friction tangent can vary linearly with V_1^2 as damage progresses. The \bar{f} dependence on \bar{V} is then established by combining (8.10)

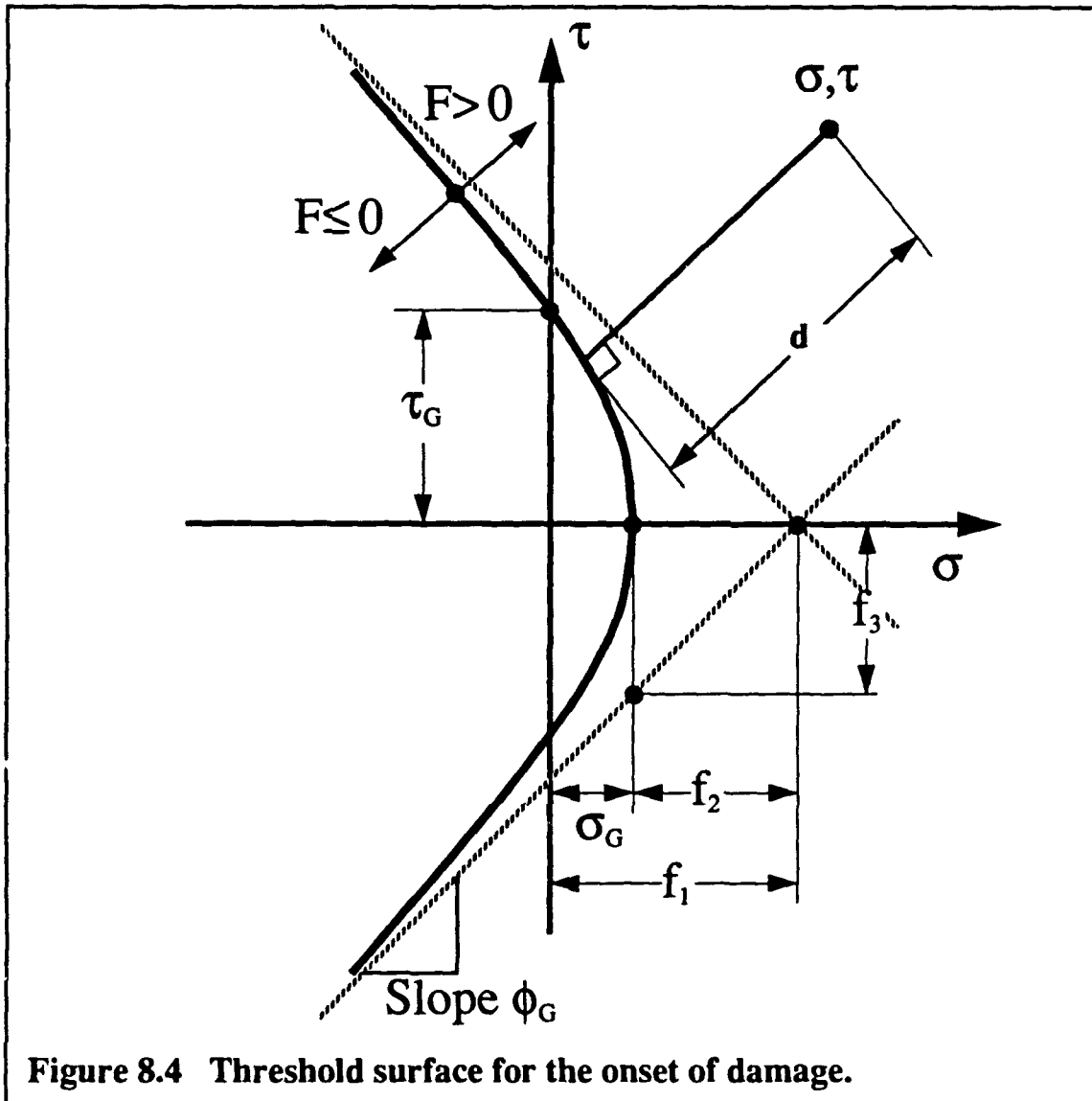


Figure 8.4 Threshold surface for the onset of damage.

and (8.12). The evolution (or rate) equations for the damage are required to complete this CDM constitutive description. For the V_1 -damage, it is further postulated that the material derivative takes the form

$$\frac{dV_1}{dt} = F_1(d_1, V_1) \quad (8.13)$$

where d_1 is the shortest distance in the $\sigma=\sigma_{11}$, $\tau=\sigma_{12}$ stress space from an exterior stress point to the threshold surface $F=0$ shown in Figure 8.4. F_1 in (8.13) should vanish for $d_1=0$, making $dV_1/dt=0$ for all stress points interior to or on the threshold surface. For purposes of illustration, (8.13) is written in the

specific power law form

$$\frac{dV_1}{dt} = (d_1/\sigma_{G10})^{n_1} [\eta_1 (1 - V_1^2)] \quad (8.14)$$

where n_1 is a positive power term for d_1/σ_{G10} , the dimensionless stress distance, η_1 is a time constant governing the rate magnitude, and the $1/(1 - V_1^2)$ term causes an acceleration of V_1 damage to complete delamination as $V_1 \rightarrow 1$. In general, the rate of damage may be a function of the location σ in the stress space and the separation from the threshold surface. For example, it could be expected that shear-induced damage under compressive stress will progress much more slowly than will tensile stress-induced damage.

The V_S in-plane isotropic damage is postulated to depend only on the stress components

$$\begin{aligned} \sigma &= \frac{1}{2} (\sigma_{22} + \sigma_{33}) \\ \tau &= \sqrt{\sigma_{12}^2 + \frac{1}{4} (\sigma_{22} - \sigma_{33})^2}. \end{aligned} \quad (8.15)$$

These quantities are derived from certain invariants of the stress tensor in absence of the σ_{11} component. This stress component has been ignored for simplification and because its effect is a sensitive function of Poisson's ratio coupling which is very uncertain at this level of approximation of material property evolution. Similarly, the σ_{22} and σ_{33} stress components were ignored in their possible effect on V_1 -damage evolution in (8.11). The stress components σ, τ in (8.15) are used in the threshold condition (8.9) to establish a distance d_S to the threshold surface. The threshold parameters \bar{f} are again given by (8.10) and the remaining quantities, to set the V_S evolution, follow. Since the V_S damage consists of an ever denser network of cracks which tends to saturate, the evolution equation for V_S is postulated to be

$$\frac{dV_S}{dt} = F_S(d_S, V_S) \quad (8.16)$$

with weak dependence on V_S . That is, no acceleration to a catastrophic failure, as in the case of $V_1 \rightarrow 1$. In fact, for purposes of illustration, take

$$\frac{dV_S}{dt} = (d_S/\sigma_{GS0})^{n_S}/\eta_S \quad (8.17)$$

with no explicit dependence on V_S and where η_S is again a time constant, d_S is normalized with the virgin growth threshold stress σ_{GS0} , corresponding to σ in (8.15), and n_S is a positive power term for the dimensionless stress distance. Saturation can be forced through the growth thresholds as

$$\begin{aligned} \sigma_{GS} &= \sigma_{GS0}/(1 - V_S^2) \\ \tau_{GS} &= \tau_{GS0}/(1 - V_S^2) \end{aligned} \quad (8.18)$$

$$\phi_{GS} = \phi_{GS0} + V_S^2(\phi_{GS1} - \phi_{GS0})$$

so that V_S damage is increasingly difficult to drive as $V_S \rightarrow 1$. This is only one possible form of the threshold functions. In the following section, another threshold form for V_S damage is considered, which may more closely represent the available experimental data.

The third mode of damage involves reinforcing fiber breakage and it may also, in general, be rate dependent due to statistical distributions of fiber strengths. For high fiber volume fraction and load aligned with the fibers, it has been found that there is very little rate dependence (see Harding and Welsh [13]). In keeping with the simplifications and assumptions which have already been made, a simple maximum strain criterion for fiber breakage is used here. It is influenced by continuum damage evolution only through the softening effects of V_1 and V_S damage upon the composite deformation.

IX. DAMAGE MODEL RESULTS FOR HOMOGENEOUS DEFORMATION

The damage model, as developed in Section VIII, is exercised for spatially homogeneous strain fields and for various strain rates and transients. Predictions are compared with experimental observations to set damage material properties and to test the versatility of the CDM approach. Composites of interest to this program do not have a strong coupling between the V_1 and V_S modes of damage due to weak Poisson's ratio coupling between the deformations which drive each of the damage types. As a result, combined damage is not expected except in biaxial or triaxial deformation fields where each mode of damage is individually driven by appropriate components of the deformation. For the sake of simplicity, and to utilize available experimental data, some simpler uniaxial deformation fields are considered in this section.

The first case to be considered involves various constant strain rates causing V_S in-plane damage. Analyses and experiments on these cases are useful to help isolate the effect of strain rate on damage and deformation. It especially should be noted that the current CDM has no explicit dependence on rates. Rather, the rate dependence will manifest itself through time required for evolution of the underlying damaging and softening processes.

The second case involves V_1 damage. Delamination, or V_1 damage, is difficult to monitor in slow rate tests and is usually absent or catastrophic such that intermediate states are rarely seen. Impact and spallation tests are most appropriate for controlled levels of delamination damage. These tests do involve wide variations of deformation rates and may be subject to qualitative judgements on the state of damage. Simulations of deformation histories expected in wave traversals are used to generate predicted damage, which is then compared with experimental evidence for spallation damage thresholds.

Constant Strain Rate Tests

Recent data has been obtained by Behler, Sikordki, and Staskewitsch [14] for graphite/epoxy composites subjected to a wide range of constant strain rate loadings. These experiments were done in a cantilever configuration with impact furnishing the higher loading rates and hydraulic loading for the lower rates. This arrangement does not precisely match the symmetries required for transversely isotropic V_S damage since these tests are approximately uniaxial flexural stress loadings with matrix cracking expected to be orientated predominately with normals parallel to the tensile stress direction. Also, these certainly are not homogeneous deformation fields. However, the comparison of experiment with CDM prediction is made anyway because it is thought that the general behavior of damage evolution in the uniaxial flexural tests may be quite similar to that for a homogeneous biaxial deformation field.

The material of most interest here, which was tested by Behler, et al [14], is a multidirectionally reinforced graphite/epoxy consisting of a balanced 0° , 90° , $\pm 45^\circ$ layup with T800 graphite fibers and Vicotex 6376 epoxy. The test specimens measured 6 mm \times 6 mm \times 45 mm. The ends of the cantilever specimens were struck with a hammer device on a flywheel which was hydraulically driven for low impact velocities (2×10^{-4} m/sec to 1 m/sec) and was electrically driven for higher impact velocities (5 m/sec to 50 m/sec). The specimens were monitored by strain gauges on the compression and tension sides and resulting strain rates ranged from $5 \times 10^{-3} \text{ sec}^{-1}$ up to 1200 sec^{-1} . While the deformation field varies through the thickness, the maximum strain and damage is expected to be localized about the outer fibers on the tension side and that response is compared with the CDM predictions. These experimental results are reproduced in Figure 9.1. Definite strengthening and stiffening with increased loading rate is seen, however, little variation in ultimate strain is indicated. The predominate softening mechanism is assumed

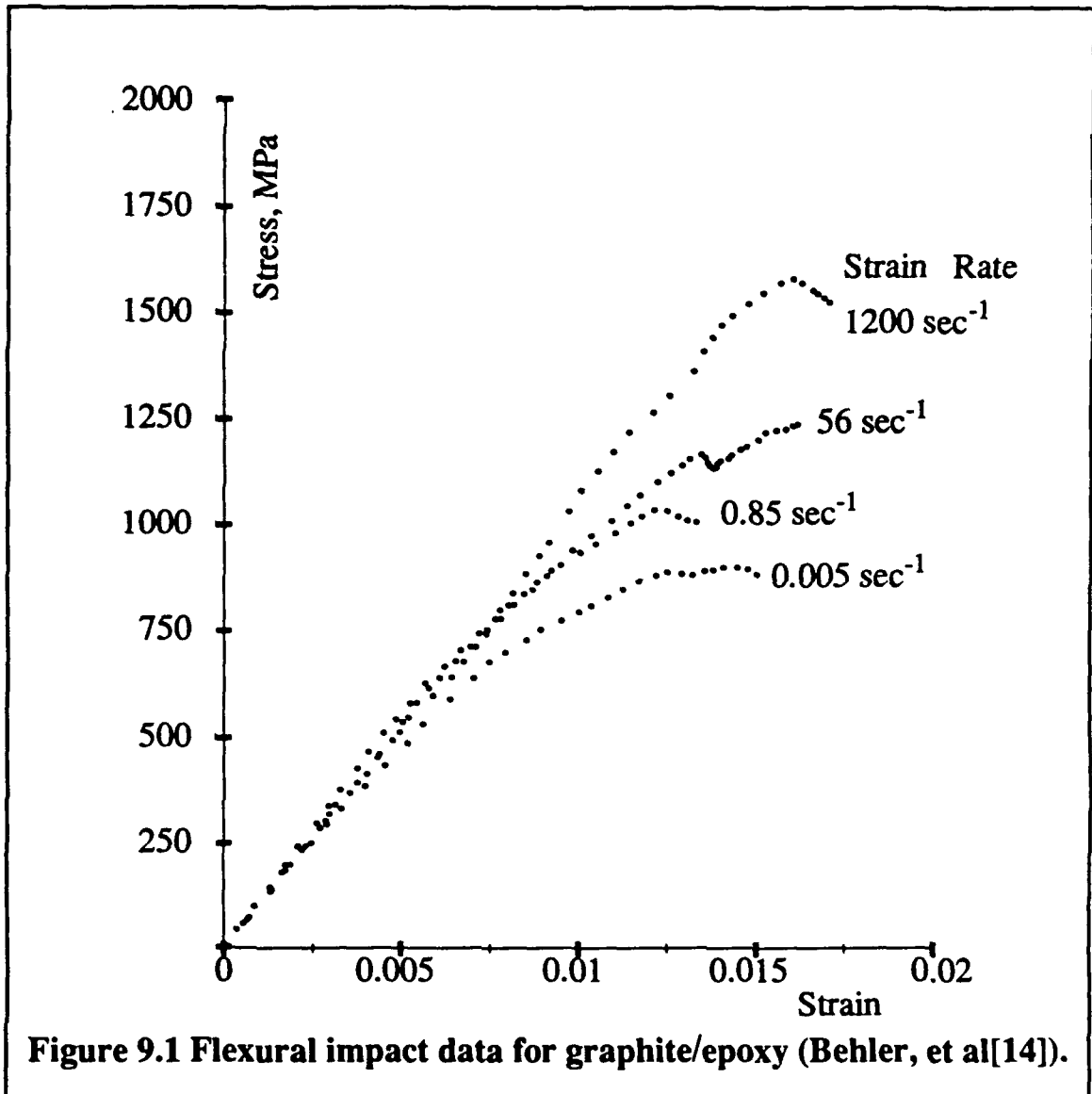


Figure 9.1 Flexural impact data for graphite/epoxy (Behler, et al[14]).

to be due to matrix cracking with only the final curvature near the breaking point being due to some evolutionary behavior in the fiber fracture.

The damage model in Section VIII is applied to biaxial deformation with $\sigma_{11}=0$ and $\epsilon_{22}=\epsilon_{33}$ with these strains being at the constant rates shown in Figure 9.1. The first attempt is with a model that has a finite threshold for the virgin state of no damage ($V_S=0$) as in (8.18) with σ_{GS0} being the initial threshold and, beyond this threshold, the damage evolves according to (8.17). The pertinent material properties are given in Table 9.1.

**Table 9.1 Material Properties for Damage
Threshold Model A**

E_{11}^0 (MPa)	10,000
E_{22}^0 (MPa)	75,000
ν_{12}^0	0.04
ν_{23}^0	0.30
$\alpha_1=\alpha_3$	0.75
α_4	0.95
n_S	1
η_S (sec)	10^{-5}
σ_{GS0} (MPa)	950

The damage Threshold Model A refers to the threshold stress in the in plane direction given by the function of damage V_S as in (8.18) or

$$\sigma_{GS} = \sigma_{GS0} / (1 - V_S^2) . \quad (9.1)$$

These properties and this threshold model are combined with the evolution equation (8.17), where for the assumed symmetries in this deformation,

$$d_S \equiv \text{Maximum} [0, \sigma_{22} - \sigma_{GS}] . \quad (9.2)$$

The elastic properties in Table 9.1 (E_{11}^0 , E_{22}^0 , ν_{12}^0 , and ν_{23}^0) are chosen to be representative of a balanced layup of graphite/epoxy. The fractional reductions (α_1 , α_3 , and α_4) are chosen very arbitrarily to attempt to reflect the elastic integrity remaining in a saturated matrix cracked state due to the intact fiber reinforcements. The exponent power was left at $n_S=1$ under the assumption that the stress, over a threshold, drives the damage. This left η_S

and σ_{GS0} as the adjustable parameters in the CDM to attempt to match the experimental results in Figure 9.1. The approach taken was to adjust the virgin threshold to account for the apparent breakpoint for softening in the fastest three loading paths. That is, the 950 MPa value in Table 9.1 represents the $\sigma_{22}=\sigma_{33}$ stress point, on initial loading, below which absolutely no V_S damage occurs. Then the rate parameter η_S was adjusted to best fit the softening behavior.

The results are shown in Figure 9.2 where the CDM prediction with Threshold Model A (defined by Table 9.1 and Equation (9.1)) are compared individually with each of the stress-strain curves from Figure 9.1. This comparison is quite favorable at high strain rates with the threshold and softening behavior allowing the predicted stress-strain curve to somewhat follow the experimental curves. Especially the 1200 sec^{-1} comparison shows a small amount of softening at the upper end, which follows the experimental data nicely. These calculations were run out to a fixed strain of 0.015 (for a rate independent fiber failure criterion) and terminated. The final stages of softening on the 1200 sec^{-1} curve may be predominately due to evolution of fiber breakage, which is not accounted for in this CDM. At rates below 0.85 sec^{-1} , the predicted curves become almost exactly bilinear and invariant with respect to rate. At these slow rates, the threshold moves with the loading and the damage evolution is in a condition of quasi-static equilibrium. That is, the damage will cease to increase immediately if the loading ceases to increase. The nonzero virgin threshold stress is seen to fail rather badly for the lowest (0.005 sec^{-1}) rate of loading, which exhibits apparent softening for any nonzero loads. These observations form the basis for another threshold model, which follows, and which attempts to more directly fit the raw data from Figure 9.1.

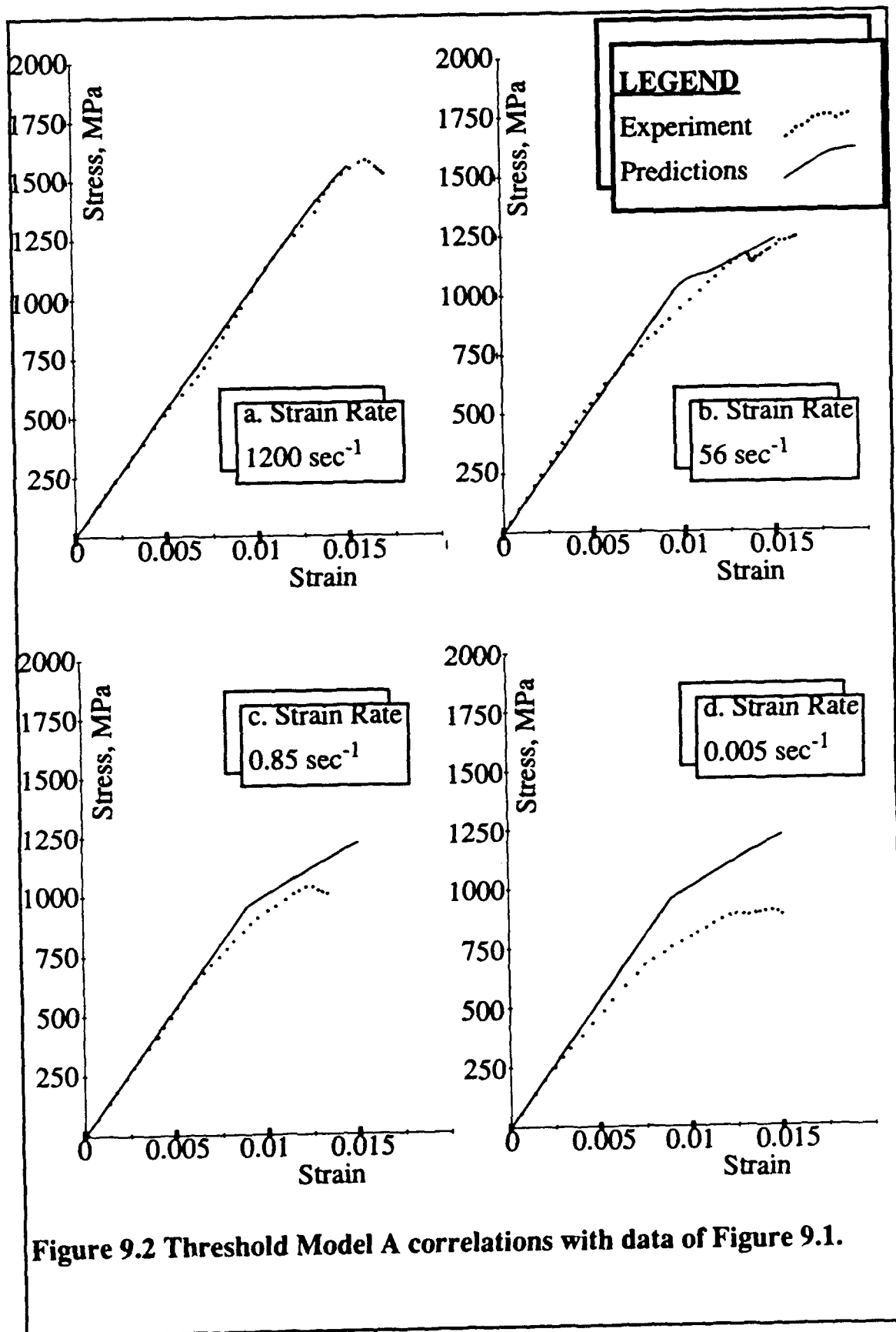


Figure 9.2 Threshold Model A correlations with data of Figure 9.1.

Since it is expected that the loading stress and the threshold stress approximately coincide for low loading rates, the 0.005 sec^{-1} data of Figure 9.1 was fit directly by a least squares routine to the threshold stress. This was done by estimating the actual damage from the reduced modulus on this loading path and then expressing the stress as a function of damage (rather than strain). The required material properties to define this model are listed in Table 9.2

Table 9.2 Material properties for Damage Threshold Model B

E_{11}^0 (MPa)	10,000
E_{22}^0 (MPa)	75,000
ν_{12}^0	0.04
ν_{23}^0	0.30
$\alpha_1 = \alpha_3$	0.75
α_4	0.95
n_S	1
η_S (sec)	0.0014
σ_{GS0} (MPa)	170

This Threshold Model B has an in-plane threshold function given by

$$\sigma_{GS} = \sigma_{GS0} V_S (1 + 31 V_S - 29 V_S^2) . \quad (9.3)$$

This form does not saturate as $V_S \rightarrow 1$ (where $\sigma_{GS} \rightarrow 3\sigma_{GS0}$), but σ_{GS} does closely follow σ_{22} for the slowest (0.005 sec^{-1}) rate loading. σ_{GS0} was adjusted to achieve this agreement and then the rate constant η_S was adjusted to best match the 56 sec^{-1} test data. In Figure 9.3, comparisons with experiment are

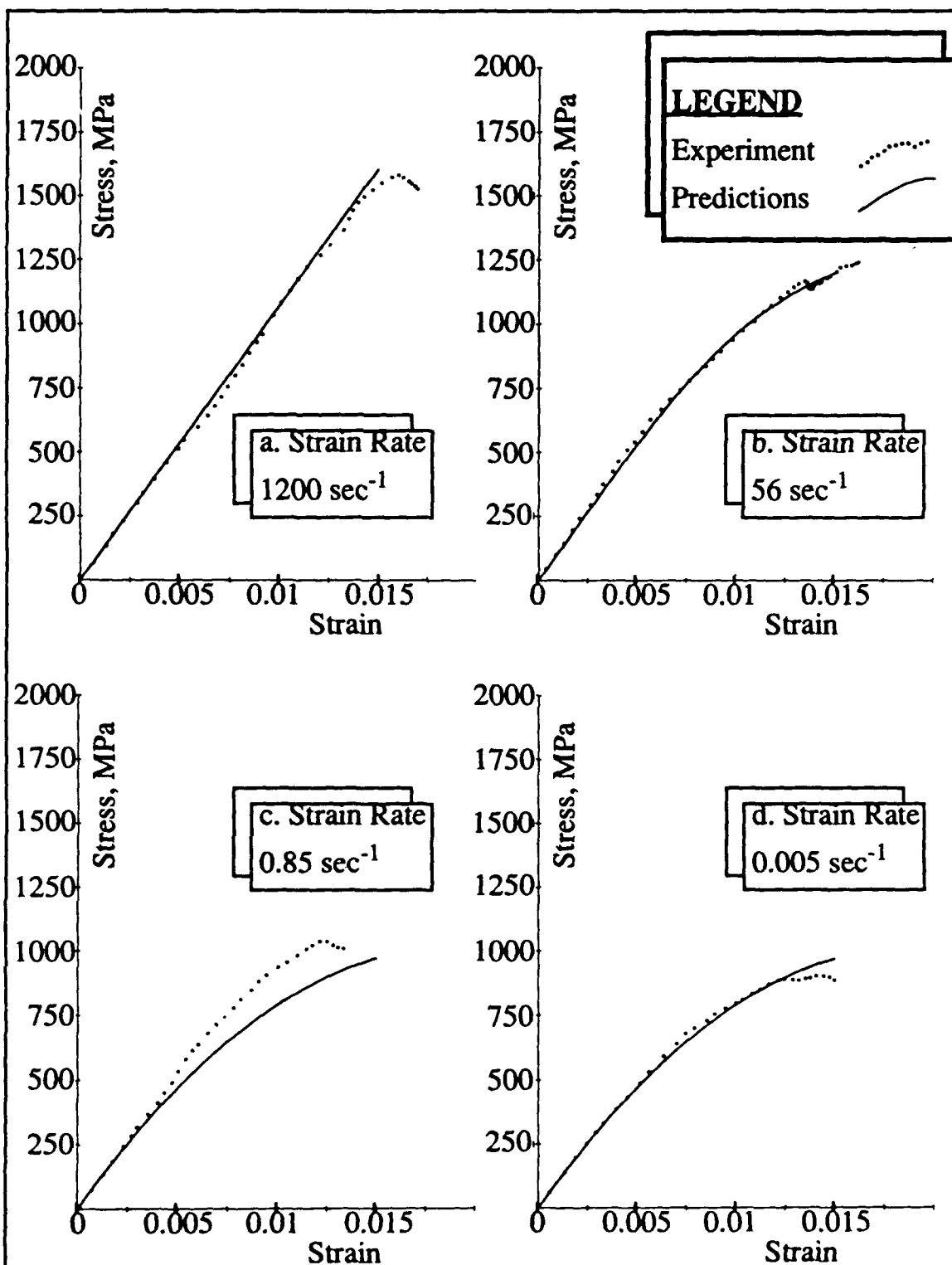


Figure 9.3 Threshold Model B correlations with data of Figure 9.1.

shown.

This Threshold Model B is seen in to fit a wide range of data very well. Deficiencies are present at the later stages of loading where fiber failure is probably dominating the detailed softening and, as in Figure 9.2, for all strain rates at least below 0.85 sec^{-1} the model predictions are invariant with respect to rate. As a result, the agreement is quite poor for the 0.85 sec^{-1} data. Possible explanations are 1) that another slow mechanism of softening should be present as an additive factor in σ_{GS} (perhaps viscoelastic deformation) or 2) that the data itself should be rate invariant at these low rates. Conclusions will have to await further experimentation and study.

Wave and Spallation Simulation

The most appropriate experiments for validation of this damage model for delamination or spallation damage, of the type shown in Figure 8.2, are planar impact by a flyer plate onto a material sample with no backing. This configuration gives rise to a transient tensile pulse due to the release wave emanating from the stress free back face. Such tests and their assessments are in progress under this program and will be reported at a later time. For the purpose of an immediate comparison of spallation predictions with experiments, Roylance [3] gave qualitative results of spallation thresholds in graphite/epoxy for variation of incident pulse shapes and those conclusions will be tested here against simulated wave deformations in the form of homogeneous fields. Roylance's results are not detailed enough to allow determination of damage variables, as was done in the preceding subsection for the V_S damage, and so only a cursory application of the model with estimated properties will be given here to demonstrate the behavior of spallation or V_1 damage predictions under transient loading.

Roylance in [3] considered a variety of graphite reinforcing fibers (Pluton,

Hercules, and Celanese) in an American Cyanamid BP907 epoxy and reported mainly longitudinal (fiber direction) properties. Transverse direction properties (1-direction from Figure 8.1) are of the most interest here for spallation damage and, hence, the epoxy bonding properties, rather than the fiber properties are thought to be most important. Indeed, Roylance found no dependence of spallation threshold on the graphite fiber type, even though the longitudinal fiber strengths and moduli were reported in [3] to vary considerably. As a result, the choice was made here to use representative graphite/epoxy properties with the realization that the following results are most sensitive to the transverse directional properties. These properties are listed in Table 9.3 along with V_1 damage properties. These damage properties

Table 9.3 Material properties for spallation simulation	
E_{11}^0 (MPa)	10,300
E_{22}^0 (MPa)	69,000
ν_{12}^0	0.04
ν_{23}^0	0.30
$\alpha_1 = \alpha_3$	0.75
α_4	0.95
n_1	2
η_1 (sec)	4×10^{-6}
σ_{G10} (MPa)	50

are being found to work well in correlating impact test data in ongoing and yet

to be reported work and they will be used here also for the purpose of illustrating the model and comparing with Roylance's results, to the extent of interpreting spallation thresholds.

Symmetries in the configuration of interest allow a reduction to uniaxial strain in the 1-direction with the first of (8.12) specifying the tensile threshold σ_{G1} and (8.14) the evolution equation for V_1 damage. In fact, the symmetries allow the distance from the damage threshold to be written as $d_1 = \text{Max}[0, \sigma_{11} - \sigma_{G1}]$. The homogeneous deformations are specified through the only nonzero strain component ϵ_{11} as a function of time for all points in space.

The first case considered is various constant strain rates from a state of zero deformation into tension. This is done to illustrate the rate-dependent behavior of the damage model and to compare with Figures 9.2 and 9.3 for V_S damage. These results are seen in Figure 9.4 where both the stress versus strain and damage versus strain are seen for a wide range of constant strain rates. Obviously both the stress and strain at failure are greatly increased as the strain rate is increased. The interpretation, in the context of this model, is that, rather than a pure rate dependence, damage evolution is lagging the application of load for the more rapid deformation. It is also observed that ultimate failure is identified as complete loss of load carrying capability through loss of modulus E_{11} in (8.7) as $V_1 \rightarrow 1$. At low strain rates (10 and 100 sec^{-1} in Figure 9.4), this model is seen to be a simplistic ultimate strength criterion with the load carrying capacity falling rapidly for $\sigma_{11} > \sigma_{G1}$.

The test conditions in Roylance's paper [3] are simulated with homogeneous deformation fields by constructing rectangular and triangular strain pulses. The compressive incident strain pulses were then augmented with the tensile release pulse from a presumed free back face and superposed as if on the

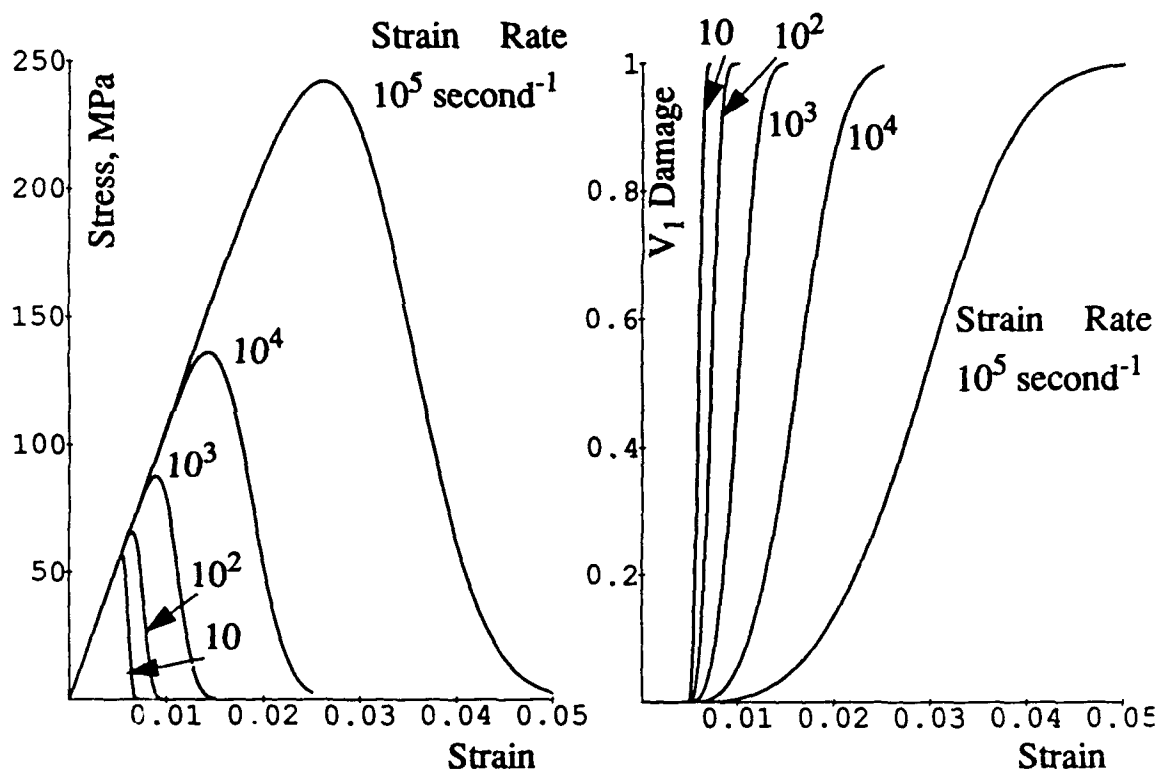


Figure 9.4 V_1 damage at various constant strain rates.

spallation plane, defined as that position nearest the back face which first feels maximum tension. This approach is somewhat simplistic and it drives the damage without feedback to the deformation field, but it does provide a prediction for softening of the elastic moduli and it is much easier to implement than is a full-blown wave propagation and damage analysis. Using the constructed strain pulses, the stress and damage histories are computed with the model. Wave propagation calculations are not really justified or appropriate for comparison with experimental results unless fairly extensive instrumentation and data acquisition has provided quantitative rather than qualitative data. Some of these more extensive analyses are presented in Section X.

Roylance considered exploding foil experiments on graphite/epoxies with

pulse shapes being approximately triangular if the pressure pulse from the explosion directly encountered the material and rectangular if the pressure pulse drove a flyer plate into the sample material. The three pulses associated with spallation thresholds were rectangular of amplitude 90 MPa and duration 1.08 μsec , rectangular of amplitude 125 MPa and duration 0.67 μsec , and triangular with amplitude 143 MPa and duration 1.42 μsec . These pulses all deliver an impulse to the material of approximately 1 kilotap (1 kilotap=1 kilobar $\cdot\mu\text{sec}$ =100 Pa $\cdot\mu\text{sec}$). Specifically, if the pulse rises (and decays for the rectangular shapes) are instantaneous, which will be assumed here, then the impulses are 0.972, 0.837, and 1.015 kilotaps, respectively, in the order listed above. These stress pulses were converted to strain deformation pulses assuming the virgin elastic properties given in Table 9.3 and the uniaxial strain symmetry condition. The strain pulses are shown in Figure 9.5 with the tensile release wave appended as expected for the deformation on the spallation plane. Also shown in Figure 9.5 are the corresponding predicted stress pulses with a slight bit of stress relaxation due to damage softening during the tensile portion of the deformation. The V_1 damage as a function of time is shown as the third transient record in Figure 9.5. Since the initial damage threshold σ_{G10} =50 MPa from Table 9.3 is obviously exceeded in each of the deformations, it is not surprising that damage does occur. It is observed that the predicted reduction in the E_{11} modulus, from Equation (8.7), is V_1^2 and only ranges from approximately 2-12%. This is, perhaps, in the appropriate range to be identified as spallation threshold, as was done by Roylance in [3]. Roylance had speculated that the approximately 1 kilotap impulse delivered in each case was indicative of an impulse criterion for spallation threshold. If the present damage model is representative of real material damage behavior, then impulse is not an appropriate criterion (accounting for the fairly wide variations in damage at approximately equal impulse) and, instead, the load sustained by the material above damage threshold controls the evolution of

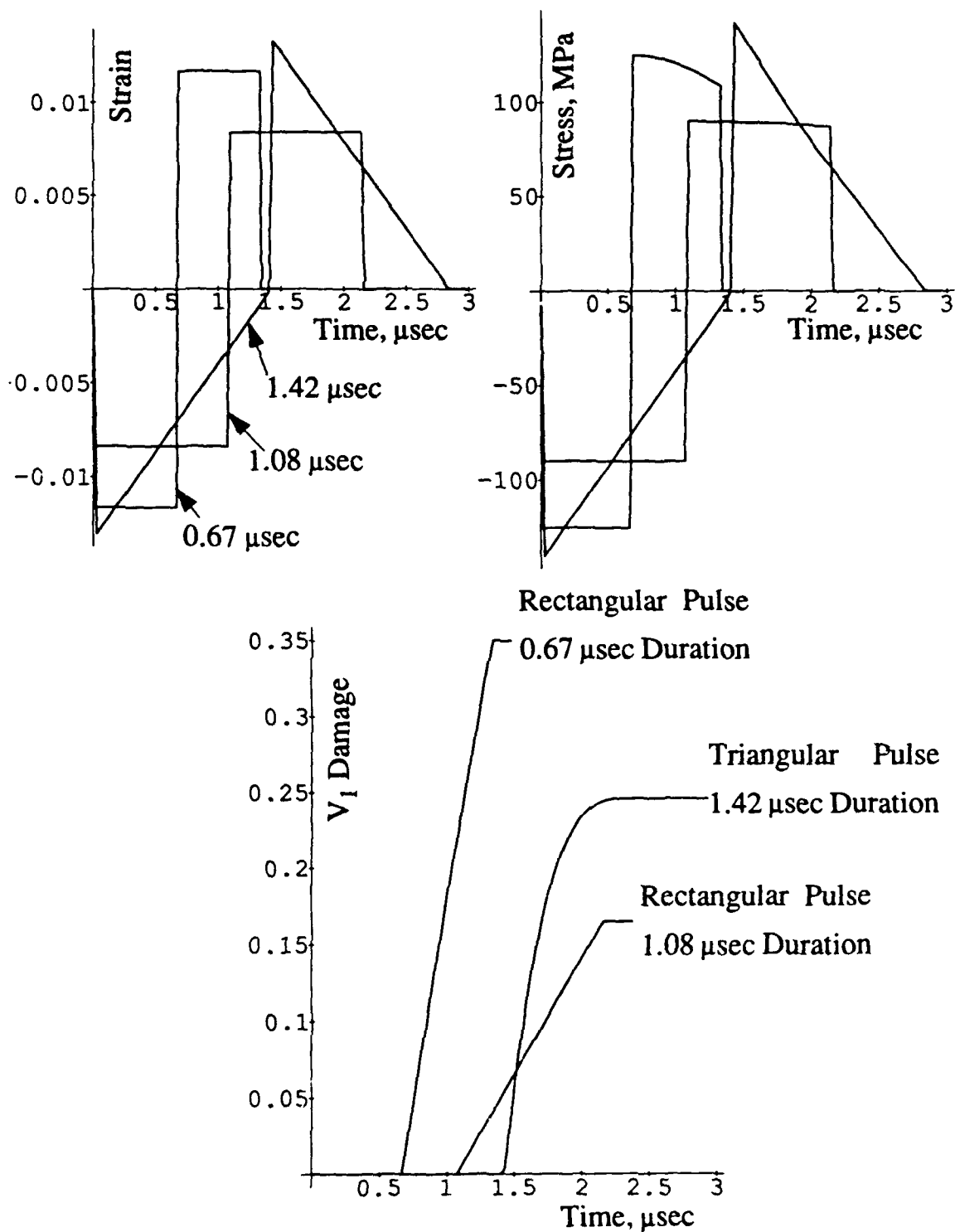


Figure 9.5 Strain, stress, and damage histories predicted for approximately 1 kilotap pulses of various shapes.

damage. Conclusions on these questions await further test results and correlations with damage models. It is concluded that softening is a very important part of the total dynamic material response and that the CDM approach is a convenient and appropriate way to handle these situations.

For the purpose of illustrating more substantial damage in a dynamic deformation, the strain deformation pulses of Figure 9.5 were magnified and the softening and damage were recalculated. These results are shown in Figure 9.6 for an impulse delivered of approximately twice that of Figure 9.5. The stress magnitudes were adjusted such that the compressive part of the pulse for all three cases delivers exactly 2 kilotaps. This is done by making the 1.08 μsec duration rectangular pulse have magnitude 185.2 MPa, the 0.67 μsec pulse have magnitude 298.5 MPa, and the 1.42 μsec triangular pulse have magnitude 281.7 MPa. It is seen in Figure 9.6 that now the softening and damage are very dramatic with rapid softening immediately upon application of substantial tensile overstress and damage levels almost completely to $V_1=1$ where the material has lost all stiffness. This inability to support large tensile stresses on the spallation plane is what alters the expected (no loss of integrity) back-face wave response (usually in the form of back face particle velocity) and forms what is called a spallation signature.

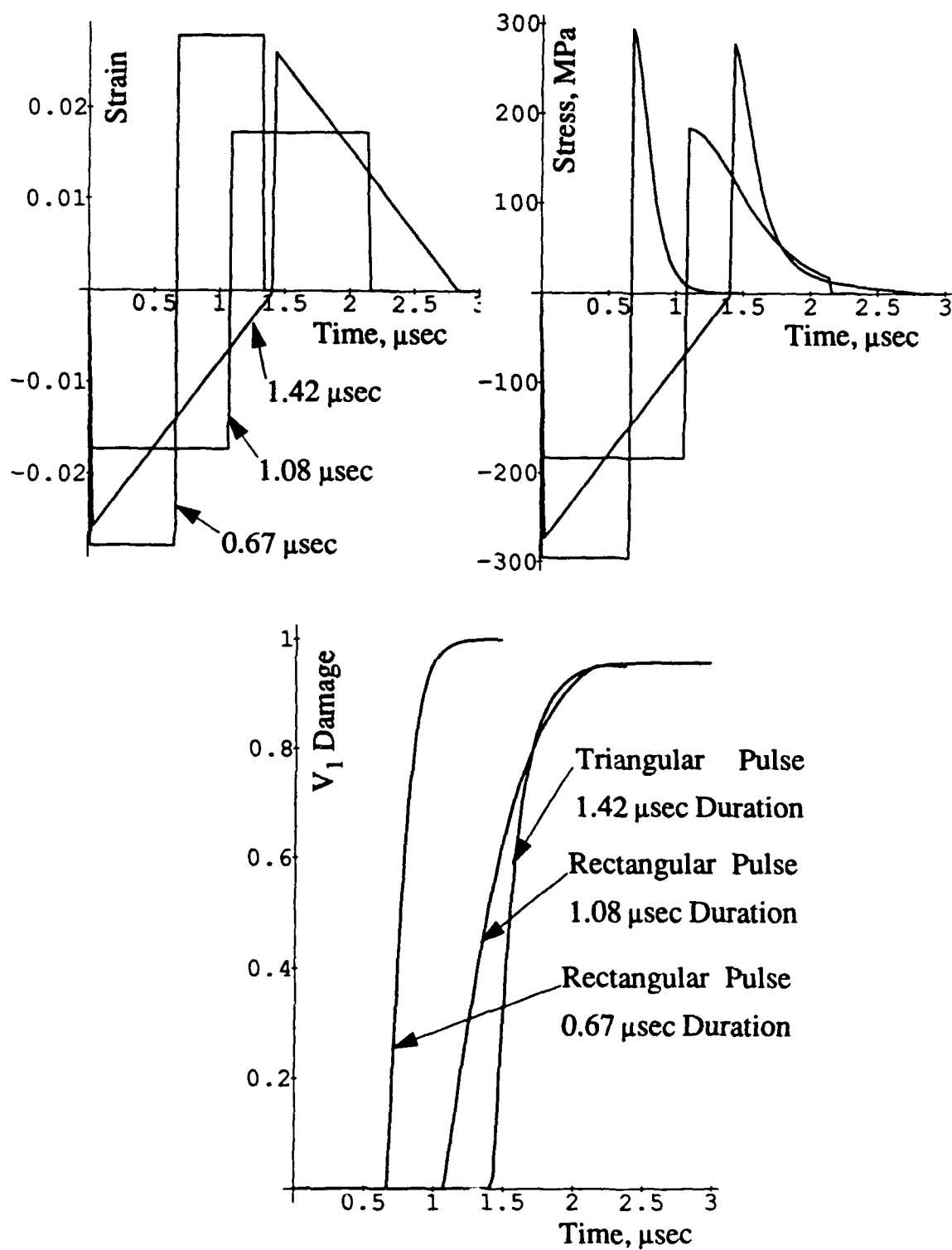


Figure 9.6 Strain, stress, and damage histories predicted for 2 kilotap pulses of various shapes.

X. PRELIMINARY APPLICATION OF DAMAGE MODEL TO TWO DIMENSIONAL PROBLEMS

In order to illustrate the application of the damage model to two dimensional axisymmetric problems, the response of the graphite/epoxy plate with diameter 267 mm subjected to shock loading from underwater explosive will be reconsidered. The material properties to be used in the simulations will be those given in Section IV for the virgin material along with the damage parameters used in Threshold Model B of Section IX. In addition to the parameters considered there, the fully two-dimensional treatment requires specification of several additional parameters related to damage under shear stresses. The parameters used here are estimated and intended principally to demonstrate application of the material model. A complete summary of the parameters used is given in Table 10.1.

As discussed in Section VI, the use of local zero displacement boundary conditions along the outer diameter of the plate results in very large stresses concentrated in that area. In order to avoid having damage occur only along the outer edge, the plate will be taken to be free in the z-direction. This results in a somewhat higher fundamental frequency of the plate than the simply supported condition considered in Section VI and lower radial stress for a given loading history. Thus, somewhat higher pressures are required to cause material damage than would be needed in a plate supported along the outer diameter.

The introduction of damage into the material constitutive behavior causes nonlinearities in the response so that use of nondimensionalized parameters in examining results as was done in Section VI is not possible. The pressure history used here is one selected to result in a level of damage in the plate to illustrate the application of the model. The pressure distribution of the incident

**Table 10.1 Material Properties for Two
Dimensional Problems**

E_{11}^0 (MPa)	10,300
E_{22}^0 (MPa)	69,000
ν_{12}^0	0.04
ν_{23}^0	0.30
G_{12}^0 (MPa)	7,170
$\alpha_1=\alpha_2=\alpha_3$	0.75
α_4	0.95
σ_{GS0} (MPa)	170
τ_{GS0} (MPa)	340
n_S	1
η_S (sec)	0.0014
$\phi_{GS1}=\phi_{GS0}$	1.0
σ_{G10} (MPa)	50
τ_{G10} (MPa)	50
n_1	2
η_1 (sec)	4×10^{-6}
$\phi_{G11}=\phi_{G10}$	0.5
ϵ_{ult}	0.015

wave applied at the surface of the fluid is chosen to produce an incident pressure at the surface of the plate at $R = 0$ of 160 MPa with a characteristic time θ_i of 0.1130 msec. The radial distribution of P and θ is then determined by Equations (5.1) and (5.3) respectively. In the first simulation the 50.8 mm thick plate is considered. Because of the presence of nonlinearity, results are presented in terms of the z -direction displacement history rather than stress history. In order to eliminate the rigid body motion component of displacement associated with the free plate, the quantity that is presented is the displacement of the center of the rear surface minus the displacement at the edge of the rear surface. The effect of damage is seen by a comparison to the plate response with the absence of damage. Figure 10.1 shows the computed

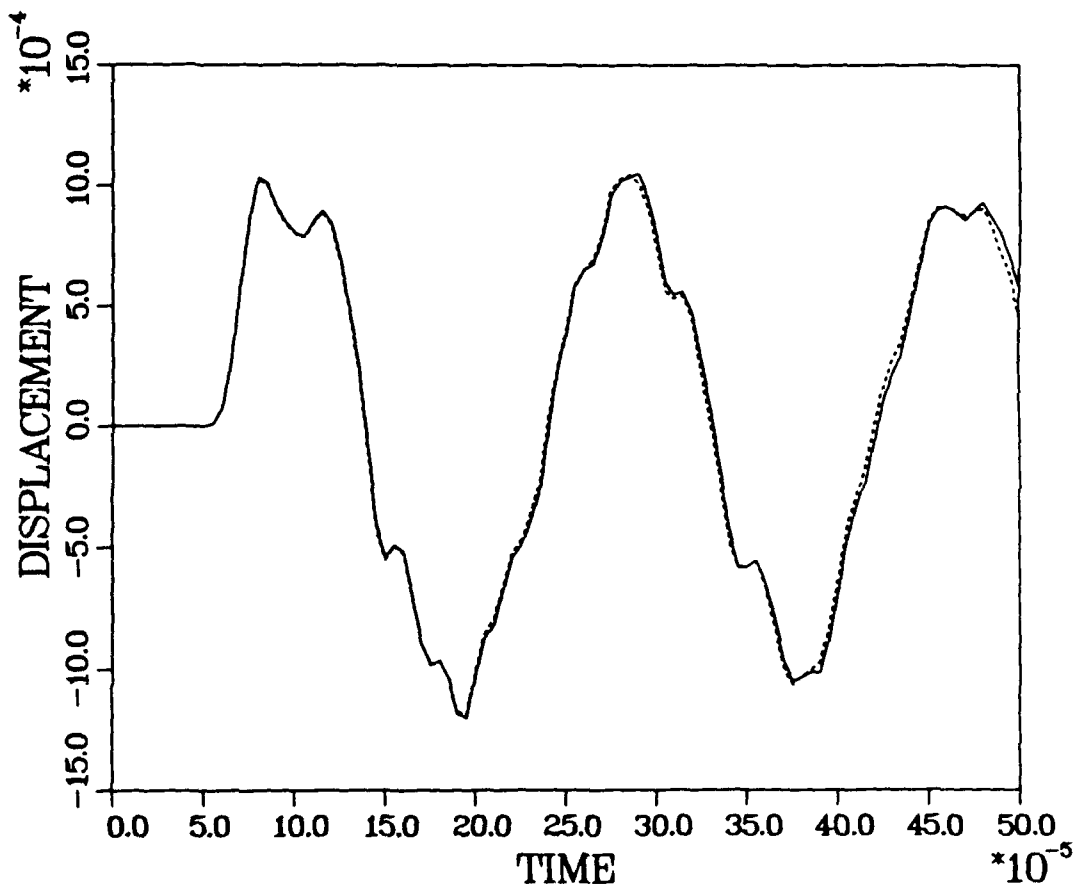


Figure 10.1 Displacement history (in meters) in 50.8 mm thick graphite/epoxy plate subjected to spherical shock wave (with damage —, without damage).

displacement history with and without the effects of damage. As seen in the figure, the response of the plate for the two computations is almost identical, indicating minimal amounts of damage. The damage contours themselves are shown in Figures 10.2 and 10.3 at a time of 500 μ s. The V_1 -damage in Figure

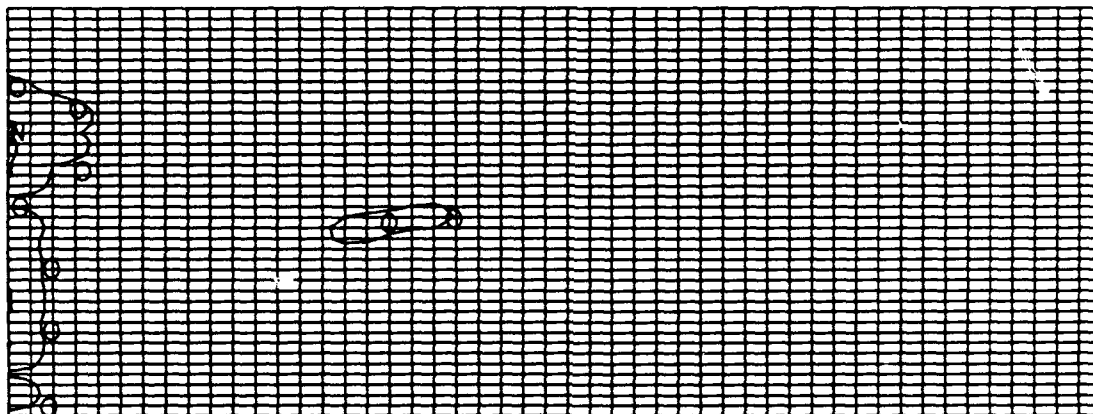


Figure 10.2 V_1 damage contours at 500 μ sec ($N=0.95$, $O=0.25$).

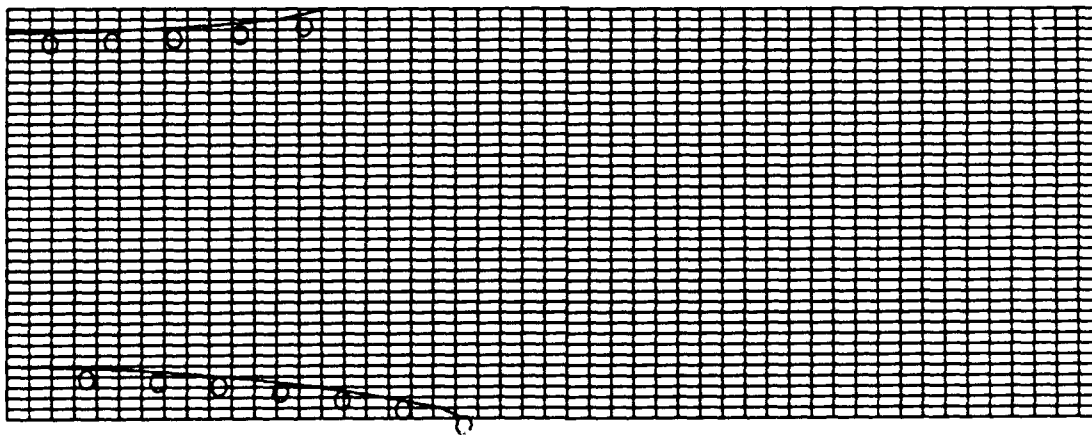


Figure 10.3 V_S damage contours at 500 μ sec ($O=0.10$).

10.2 is concentrated near the z -axis, where the direct through thickness tensile stresses are greatest and shear stress is minimal indicating that the

delamination damage occurs from the stress waves propagating through the thickness of the material. The contour shown is for a value of 0.25, which represents a sub-spallation condition, with some reduction in the material stiffness. The V_S -damage contour is shown in Figure 10.3. As expected the damage occurs at the upper and lower surface of the plate near the center as the plate oscillates, producing alternating tension and compression on each face. Again though, the level of the damage is fairly low so that the reduction of stiffness is not substantial, which is consistent with the minor differences noted in the displacement history.

In the next simulation the effect of a higher level of damage is considered. A 25.4 mm thick plate subjected to a shock wave of twice the amplitude as the previous simulation, but retaining the same spatial and temporal distribution, will be investigated. The same measure of displacement will be used to study the effect of damage on the plate response. The displacement history for the simulation is shown in Figure 10.4. Here it can be seen that the damage has greatly influenced the response of the plate after the initial oscillation. The stiffness has been reduced to such extent that the displacements at the time of 400 μsec for the plate with and without damage are almost completely out of phase.

The distribution of damage is examined at both early and late time. The V_1 -damage distribution is shown in Figure 10.5 at a time of 125 μsec . Contours

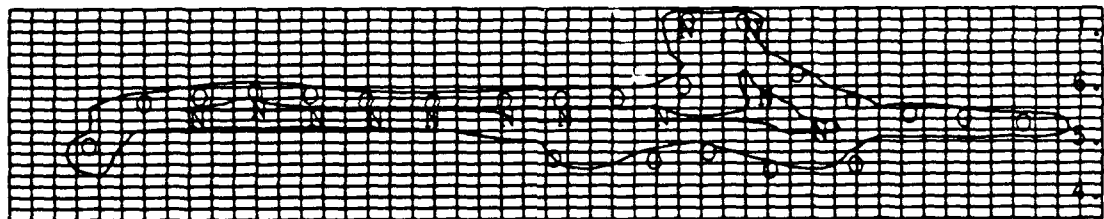


Figure 10.5 V_1 damage contours at 125 μsec ($N=0.95$, $O=0.25$).

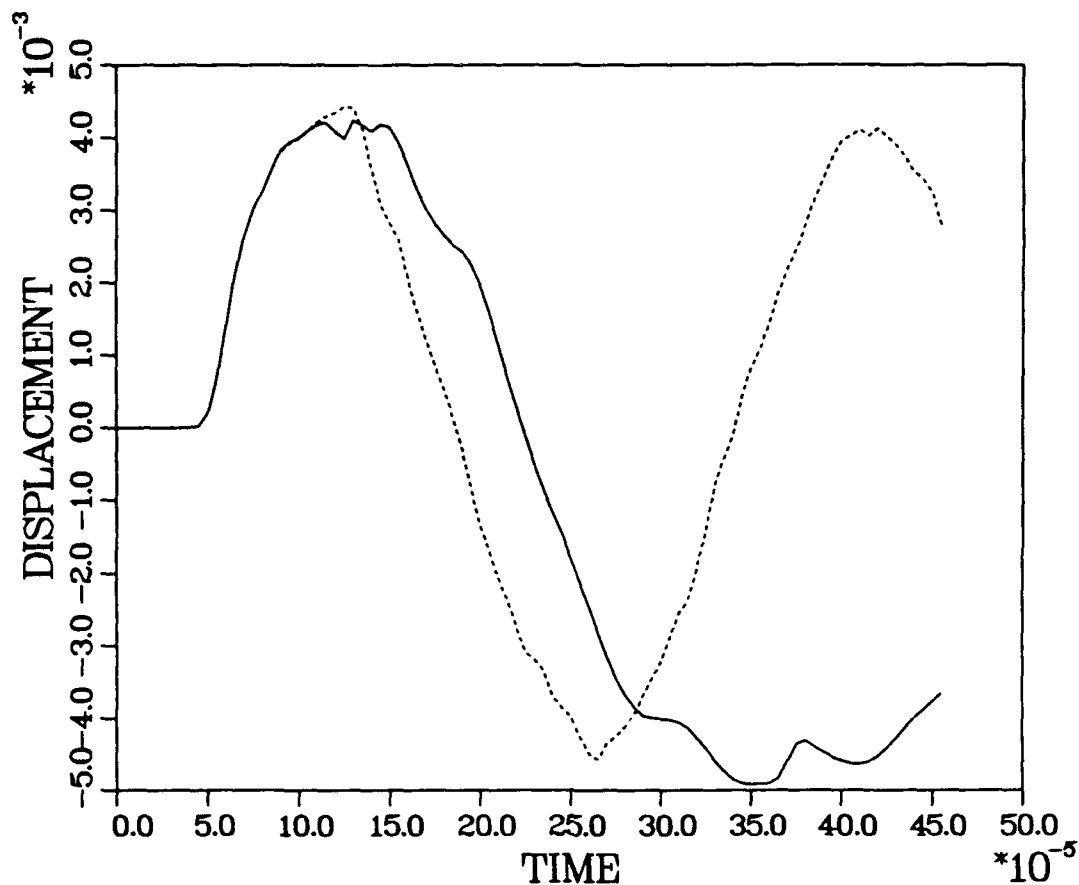


Figure 10.4 Displacement history (in meters) in 25.4 mm thick graphite/epoxy plate subjected to spherical shock wave (with damage —, without damage).

are shown for two levels of damage, one representing onset or partial damage and one representing delamination. As seen in the figure, there is no damage along the z-axis, indicating that the damage is a result of shear stresses not the through-thickness tensile stresses as was the case in the 50.8 mm thick plate. The contours of the V_S -damage are shown in Figure 10.6. At this time tension

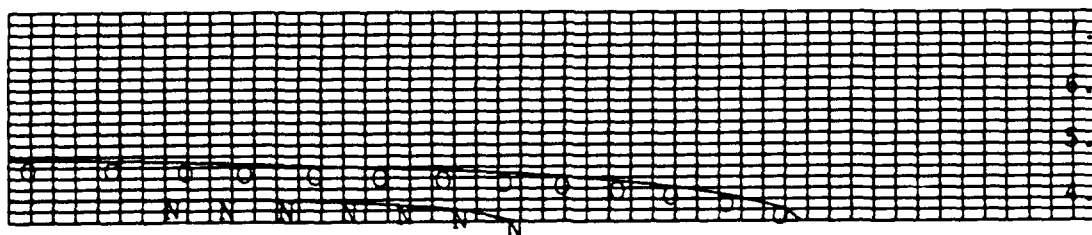


Figure 10.6 V_S damage contours at 125 μs ($N=0.1$, $O=0.05$).

has only occurred on the rear surface of the plate, thus there is no V_S -damage on the front surface. The V_1 and V_S damage contours at 500 μsec are shown in Figures 10.7 and 10.8, respectively. Examination of the damage contours

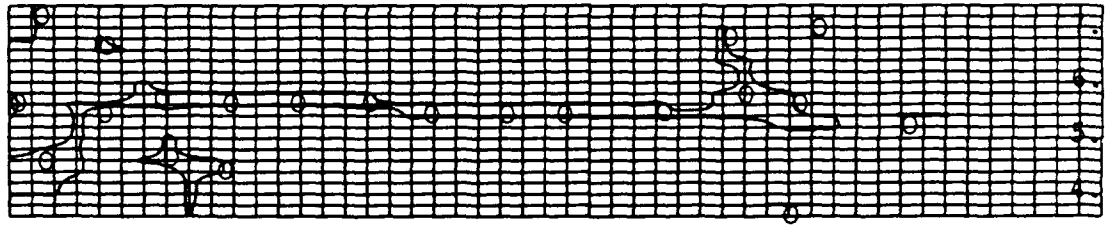


Figure 10.7 V_1 damage contours at 500 μsec ($O=0.95$).

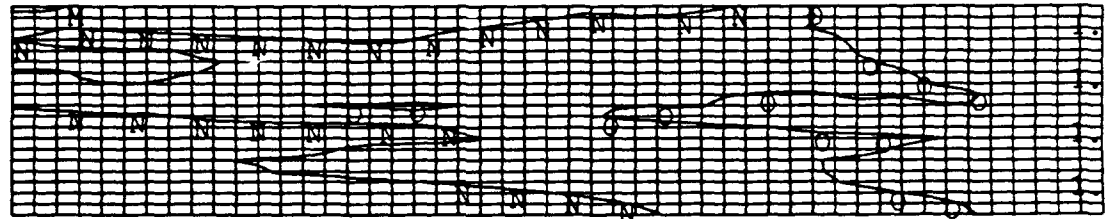


Figure 10.8 V_S damage contours at 500 μsec ($N=0.10$, $O=0.05$).

shows that the delamination or V_1 damage extends almost entirely across the radius of the plate (in effect saying that complete delamination has occurred), thus preventing shear transfer through the thickness.

The final example to be considered is for the 50.8 mm thick plate subjected to 320 MPa with the same $\theta_t=0.1130$ msec. The V_1 -damage contours are shown at the time of 500 μsec in Figure 10.9. As seen in Figure 10.9, there is a large region of delamination damage near the z axis and also one approximately at two thirds of the plate radius. The first of these is attributed to the through-thickness tensile stresses that develop while the second region is attributed to shear stresses since this is a region of inflection in the plate bending. This can also be seen by examining the deformed geometry of the plate in Figure 10.10

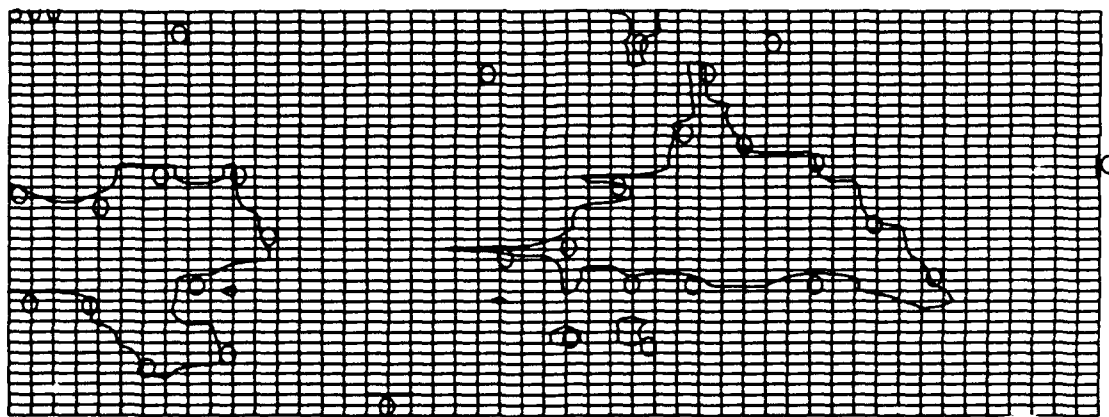


Figure 10.9 V_1 damage contours at 500 μsec ($O=0.95$).

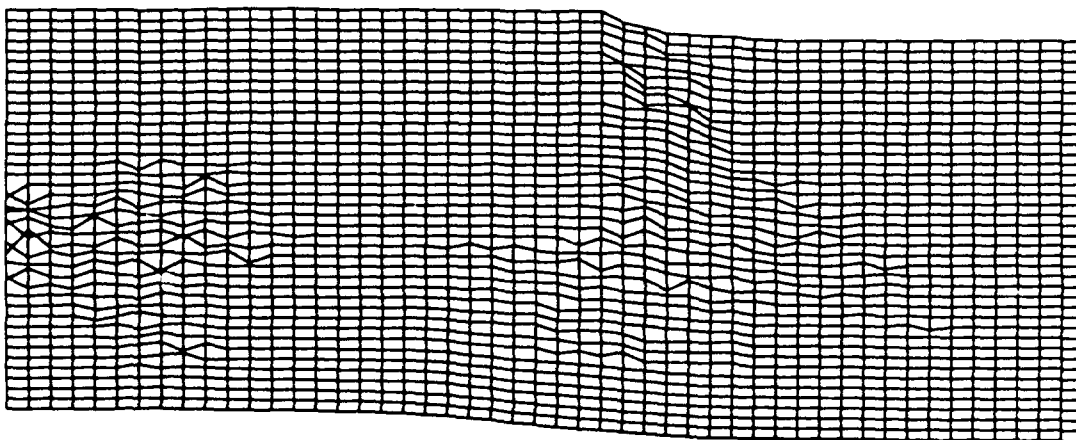


Figure 10.10 Deformed geometry of 50.8 mm thick graphite/epoxy plate subjected to spherical shock wave.

at the time of 500 μsec . The central portion of the plate shows a region disturbed by damage corresponding to the first contour of critical damage. As $V_1 \rightarrow 1$ several of the material coefficients go to zero, which permits the material to deform extensively under very small loads, resulting in the distorted region seen in the figure. The other region of high V_1 damage is manifested by the large shear distortion seen across the thickness of the plate. The softening of the material with damage results in a localized band in which the distortion takes place somewhat analogous to the shear bands seen in metals under shear deformation.

XI. SUMMARY

This report has concentrated on the early time material response of thick composite plates by presenting the development and demonstration of techniques and models appropriate for response predictions and experimental correlation. Various levels of theoretical and numerical prediction techniques are compared with available experimental data and with each other. The time and space regimes of interest for shock wave damage clearly include both body wave response and early flexural and shear vibration modes when two-dimensional plate configurations are considered. Finite-element calculations are presented which show direct through-thickness wave arrivals which transition into flexural vibrations as time progresses. Specific findings are listed below.

The results presented indicate that the use of continuum finite elements in conjunction with silent boundary conditions to represent the fluid is an appropriate modelling technique, at least for two-dimensional problems. The technique allows for the effects of material nonlinearity and cavitation to be included without a tremendous computational penalty. The results indicate, however, that a more refined mesh than that considered here should be used for comparing computational results to actual experiments or for predictions of component response, particularly where through thickness stress is important. For predominately flexural behavior the modelling technique employed gave results which agreed extremely well with analytical results.

The use of zero displacement boundary conditions at the edge of the plates results in very high local stresses. For cases of modelling

a composite material EBT, an attempt to simulate the actual plate support conditions, as much as is feasible, should be made. Use of contact surfaces may be beneficial.

Results of calculations of spherical shock waves on steel and graphite/epoxy plates show that the momentum density transmitted to the graphite epoxy plate is approximately 50% less than that transmitted to the steel plate due to its lower mechanical impedance. This is significant since this momentum density must be resisted by the radial stresses in the plate. The calculations also show that for plates of 267 mm diameter and 25.4 mm thickness the displacement of the graphite/epoxy is approximately twice that of the steel, but at one fifth the weight, which demonstrates a distinct advantage of the composite material. However, due to the relatively slow wave speed in the through thickness direction of the composite plate, tensile stresses develop even under spherical waves. These tensile stresses are particularly significant due to the low transverse strength of the composite, indicating that spallation in the thick composite is a possible damage mode.

A continuum damage model was developed for application to thick composite materials subjected to high-rate dynamic loading. The model is capable of describing the rate dependent, nonlinear behavior of the composite material. The model compares favorably to the limited available experimental data at high rates for cases of idealized homogeneous deformation.

Preliminary application of the model to multi-dimensional problems was performed to illustrate its capability. The results

obtained appear reasonable, but were not compared to experiments due to lack of available data. There also are a number of parameters in the model that are difficult to determine and thus far have been estimated, with some parametric studies conducted to assess the sensitivity of the results. Even with these difficulties the model appears to be a very promising step to describe the material response under these transient loadings.

This work is supported by the DARPA Naval Technology Office and that support is greatly appreciated.

REFERENCES

1. R.K. Kapania and S. Raciti, "Recent Advances in Analysis of Laminated Beams and Plates, Part II: Vibrations and Wave Propagation," AIAA Journal, Vol.27, No. 7, 1989, pp. 935-946.
2. K.M. Wu, "Preliminary Modeling of Compressive Shock and Spallation in Thick Composite Materials," NRL Memorandum Report 6684, 1990.
3. D. Roylance, "Stress-Wave Damage in Graphite/Epoxy Laminates," J. Comp. Mat. Vol. 14, 1980, pp.111-119.
4. R.E. Tokheim, D.C. Erlich, T. Kobayashi, and J.B. Aidun, "Characterization of Spall in Kevlar/Epoxy Composite," in Shock Compression in Condensed Matter, 1989, Eds.S.C. Schmidt, et al., Elsevier Science publishers B.V., 1990, pp. 473-476.
5. E.C. Goeke and F.A. McClintock, "Fracture of Graphite Composites Under Shock Loading," J of Appl. Phys., Vol. 46, No. 11, 1975, pp. 4671-4673.
6. L.J. Cohen and H.M. Berkowitz, "Dynamic Fracture of a Quartz-Phenolic Composite Under Stress-Wave Loading in Uniaxial Strain," Franklin Institute Journal Vol. 293, No. 1, 1972, pp. 25-45
7. W.S. Pellini, "Use and Interpretation of the NRL Explosion Bulge Test," NRL Memorandum Report 4034, 1952.
8. P.P. Puzak and W.S. Pellini, "Standard Evaluation Procedures for Explosion Bulge Testing (Weldments)," NRL Memorandum Report 1255, 1961.
9. J.H. Giovanola, R.W. Klopp, J.W. Simons, and A.H. Marchand, "Investigation of the Fracture Behavior of Scaled HY-130 Steel Weldments,"

SRI International Report PYU-2612, 1990.

10. K. Wong and J. Ahmad, "Inelastic Dynamic Finite Element Fracture Mechanics Analysis of Submarine Explosion Bulge Panels, Phase I," DREA Report No. DREA/CR/89/431, 1989.

11. NRL Contract No N00014-86-C-2580.

12. R.A. Jones, "The Response and Failure Mechanisms of Circular Metal and Composite Plates Subjected to Underwater Shock Loading," M.S. Thesis, Naval Postgraduate School, 1990.

13. J. Harding and L.M. Welsh, "A Tensile Testing Technique for Fibre-Reinforced Composites at Impact Rates of Strain," J. Mat. Sci. Vol. 18, 1983, pp. 1810-1826.

14. F.J. Behler, S. Sikorski, and E. Staskewitsch, International Conf. on Shock-Wave and High Strain Rate Phenomena in Materials, Aug. 12-17, 1990, San Diego, CA.

15. L.M. Taylor and D.P. Flanagan, "PRONTO 2D, A Two-dimensional Transient Solid Dynamics Program," SAND86-0594, 1987.

16. S.W. Tsai, Composites Design, 1986, Think Composites, Dayton, OH, 1986.

17. T.L. Geers, "Transient Response Analysis of Submerged Structures," in Finite Element Analysis of Transient Non-linear Behavior AMD Vol. 14, New York, 1975.

18. R.H. Cole, Underwater Explosions, Princeton Univ. Press, Princeton, N.J., 1948.

19. A.B. Arons, J. Acoust. Soc. Am., Vol. 26, 1954, pp. 343-345.
20. P.H. Rogers, "Weak-shock Solution for Underwater Explosive Shock Waves," J. Acoustic Soc. Am., Vol. 62, No. 6, 1977.
21. T. Belytschko, "An Overview of Semidiscretization and Time Integration Procedures," in Computational Methods for Transient Analysis, Eds. T. Belytschko and T.J.R. Hughes, North-Holland, Amsterdam, 1983.
22. D.P. Flanagan and T. Belytschko, "A Uniform Strain Hexahedron and Quadrilateral with Orthogonal Hourglass Control," Int. J. Numer. Meth. Eng., Vol. 17, 1981, pp. 679-706.
23. J. von Neumann and R.D. Richtmyer, "A Method for the Numerical Calculation of Hydrodynamic Shocks," J. Appl. Phys., Vol. 21, No. 3, 1950, pp. 232-237.
24. J. Lysmer and R.L. Kuhlemeyer, "Finite Dynamic Model for Infinite Media," J. Eng. Mech. Div. ASCE, 1979, pp. 859-877.
25. M. Cohen and P.C. Jennings, "Silent Boundary Methods," in Computational Methods for Transient Analysis, Eds. T. Belytschko and T.J.R. Hughes, North-Holland, Amsterdam, 1983.
26. L.M. Barker, "A Model for Stress Wave Propagation in Composite Materials," Vol. 5, 1971, pp. 140-162.
27. H. Huang, "Transient Bending of a Large Elastic Plate by a Spherical Pressure Wave," J. Appl. Mech., Vol. 41, 1974, pp. 772-776.
28. R.D. Mindlin, "Influence of Rotatory Inertia and Shear on Flexural Motions of Isotropic Elastic Plate," J. Appl. Mech., Vol. 18, 1951, pp. 31-38.

29. L. Davison and A. L. Stevens, "Thermomechanical Constitution of Spalling Elastic Bodies," J. Appl. Phys., Vol. 44, No. 2, 1973, pp. 668-674.
30. D. Krajcinovic, "Damage Mechanics," Mechanics of Materials, Vol. 8, 1989, pp. 117-197.
31. R. Talreja, "A Continuum Mechanics Characterization of Damage in Composite Materials," Proc. R. Soc., Vol. A399, 1985, pp. 195-216.
32. D. R. Curran, L. Seamen and D. A. Shockey, "Dynamic Failure of Solids," Physics Reports, Vol. 147, 1987, pp. 253-388.